



AFRL-AFOSR-JP-TR-2016-0099

---

## Robust Adaptive Flight Control Design of Air-breathing Hypersonic Vehicles

Radhakant Padhi  
INDIAN INSTITUTE OF SCIENCE

---

12/07/2016  
Final Report

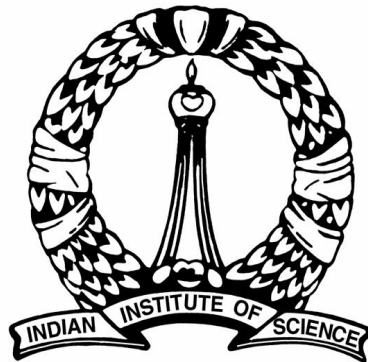
DISTRIBUTION A: Distribution approved for public release.

Air Force Research Laboratory  
AF Office Of Scientific Research (AFOSR)/ IOA  
Arlington, Virginia 22203  
Air Force Materiel Command

<b>REPORT DOCUMENTATION PAGE</b>				Form Approved OMB No. 0704-0188	
<p>The public reporting burden for this collection of information is estimated to average 1 hour per response, including the time for reviewing instructions, searching existing data sources, gathering and maintaining the data needed, and completing and reviewing the collection of information. Send comments regarding this burden estimate or any other aspect of this collection of information, including suggestions for reducing the burden, to Department of Defense, Executive Services, Directorate (0704-0188). Respondents should be aware that notwithstanding any other provision of law, no person shall be subject to any penalty for failing to comply with a collection of information if it does not display a currently valid OMB control number.</p> <p>PLEASE DO NOT RETURN YOUR FORM TO THE ABOVE ORGANIZATION.</p>					
1. REPORT DATE (DD-MM-YYYY) 07-12-2016		2. REPORT TYPE Final		3. DATES COVERED (From - To) 26 May 2015 to 25 May 2016	
4. TITLE AND SUBTITLE Robust Adaptive Flight Control Design of Air-breathing Hypersonic Vehicles				5a. CONTRACT NUMBER	
				5b. GRANT NUMBER FA2386-15-1-4045	
				5c. PROGRAM ELEMENT NUMBER 61102F	
6. AUTHOR(S) Radhakant Padhi				5d. PROJECT NUMBER	
				5e. TASK NUMBER	
				5f. WORK UNIT NUMBER	
7. PERFORMING ORGANIZATION NAME(S) AND ADDRESS(ES) INDIAN INSTITUTE OF SCIENCE SCIENCE INSTITUTE BANGALORE, 560012 IN				8. PERFORMING ORGANIZATION REPORT NUMBER	
9. SPONSORING/MONITORING AGENCY NAME(S) AND ADDRESS(ES) AOARD UNIT 45002 APO AP 96338-5002				10. SPONSOR/MONITOR'S ACRONYM(S) AFRL/AFOSR IOA	
				11. SPONSOR/MONITOR'S REPORT NUMBER(S) AFRL-AFOSR-JP-TR-2016-0099	
12. DISTRIBUTION/AVAILABILITY STATEMENT A DISTRIBUTION UNLIMITED: PB Public Release					
13. SUPPLEMENTARY NOTES					
14. ABSTRACT Two robust adaptive nonlinear controller designs are presented in this report for control of an air-breathing hypersonic vehicle in the cruise phase of flight. The first type of controller uses dynamic inversion and the second one is obtained using newly developed state-constrained generalized dynamic inversion technique with the help of Lyapunov theory. Furthermore, the robustness of both controllers is enhanced by augmenting them with a fast disturbance observer.					
15. SUBJECT TERMS Hypersonic Flight Control					
16. SECURITY CLASSIFICATION OF:			17. LIMITATION OF ABSTRACT  SAR	18. NUMBER OF PAGES 67	19a. NAME OF RESPONSIBLE PERSON KNOPP, JEREMY
a. REPORT Unclassified	b. ABSTRACT Unclassified	c. THIS PAGE Unclassified			19b. TELEPHONE NUMBER (Include area code) 315-227-7006

# Robust Adaptive Flight Control Design of Air-breathing Hypersonic Vehicles

Report No. IISc/CSIC/AE/RP/AOARD/2016



Kapil Sachan, Radhakant Padhi  
Department of Aerospace Engineering  
Indian Institute of Science  
Bangalore, 560012, INDIA

# Abstract

Two robust adaptive nonlinear controller designs are presented in this report for control of an air-breathing hypersonic vehicle in the cruise phase of flight. The first type of controller uses dynamic inversion and the second one is obtained using newly developed state-constrained generalized dynamic inversion technique with the help of Lyapunov theory. Furthermore, the robustness of both controllers is enhanced by augmenting them with a fast disturbance observer.

The controller is derived using dynamic inversion technique, by transforming nonlinear system dynamics into linear system dynamics with the help of transformation matrix. Further, the control expression is obtained using stable linear error dynamics, which ensures the asymptotic stability of the error. However, a perfectly known system is assumed while designing the controller using dynamic inversion, which is very difficult to achieve in the case of air-breathing hypersonic vehicle. Hence, constrained neuro-adaptive dynamic inversion technique with Jacobian learning approach is proposed in this report. In this technique, an unknown disturbance function is learned by the controller along with the Jacobian matrix of the unknown disturbance to ensure fewer transients. Further, barrier Lyapunov function is used in the formulation of neuro-adaptive dynamic inversion technique to constrain the error in disturbance learning.

The state-constrained generalized dynamic inversion technique is formulated using Barrier Lyapunov function in this report. Further, the derived controller is robust enough to maintain the states within the constrained bounds in presence of unknown disturbances or model uncertainties. However, the perfect tracking is achieved by augmenting the state-constrained generalized dynamic inversion with constrained neuro-adaptive Jacobian matrix learning based disturbance learning mechanism.

Further, six degree-of-freedom winged-cone air-breathing hypersonic vehicle model is used in this report to demonstrate the performance of derived controllers. Moreover, the uncertainties are assumed in aerodynamic coefficients and inertia components of the vehicle model. Further, it has been shown that the proposed controllers are robust enough to take care of model uncertainties or any bounded unknown external disturbance function affecting the air-breathing hypersonic vehicle dynamics. Along with the stabilization of uncertain air-breathing hypersonic vehicle, the controllers also prevent inlet unstart. It has also been shown that the proposed controllers can perfectly tolerate up to 30% parameter uncertainties and disturbances. Moreover, using Monte-Carlo simulations, the quantitative results of the performance of proposed controllers in presence of model uncertainties are also presented in this report. Finally, the applicability of the proposed control techniques is illustrated by promising simulation results.

# Contents

## Abstract

<b>List of figures</b>	<b>iii</b>
------------------------	------------

<b>List of tables</b>	<b>vi</b>
-----------------------	-----------

<b>1 Introduction</b>	<b>1</b>
-----------------------	----------

1.1 Motivation . . . . .	1
--------------------------	---

1.2 Literature Survey . . . . .	3
---------------------------------	---

1.3 Control Objectives . . . . .	5
----------------------------------	---

<b>2 Hypersonic Vehicle Model Selection and Vehicle Dynamics</b>	<b>7</b>
--	----------

2.1 Vehicle Dynamics . . . . .	7
--------------------------------	---

2.2 Forces and Moments Calculation . . . . .	11
--	----

<b>3 Nominal Dynamic Inversion Control Design of Hypersonic Vehicle</b>	<b>15</b>
---	-----------

3.1 Outer Loop Control design . . . . .	15
---	----

3.2 Intermediate Loop Control design . . . . .	17
--	----

3.3 Inner Loop Control design . . . . .	17
---	----

3.4 Velocity Loop Control design . . . . .	18
--	----

3.5 Simulation Results . . . . .	19
----------------------------------	----

3.5.1 Calculation of Trim Conditions . . . . .	19
--	----

3.5.2 Simulation results . . . . .	19
------------------------------------	----

<b>4 Neuro-adaptive Dynamic Inversion with Jacobian Learning</b>	<b>28</b>
--	-----------

4.1 Neuro-adaptive Dynamic Inversion Control Formulation . . . . .	28
--	----

<i>CONTENTS</i>	iii
4.2 Constrained Weight Update Rule with Jacobian Learning . . . . .	29
4.3 Simulation Results . . . . .	31
<b>5 Neuro-adaptive Generalized Dynamic Inversion with Jacobian Learning</b>	<b>39</b>
5.1 Neuro-adaptive State-constrained Generalized Dynamic Inversion Formulation	39
5.1.1 Formulation of State-Constrained Generalized Dynamic Inversion . . .	39
5.1.2 Neuro-adaptive SC-GDI Control Formulation . . . . .	43
5.2 Simulation Results . . . . .	43
5.3 Quantitative Comparison Between Neuro-adaptive DI and GDI . . . . .	51
<b>6 CONCLUSION</b>	<b>52</b>
<b>Bibliography</b>	<b>56</b>

# List of Figures

1.1	Mission Scenario . . . . .	6
2.1	Air-breathing Hypersonic Vehicle Geometry [Shaughnessy et al., 1990] . . . . .	8
3.1	Block Diagram of Three-Loop-Control Design . . . . .	16
3.2	Mach Number ( $M$ ), Angle of Attack ( $\alpha$ ) and Sideslip Angle ( $\beta$ ) Profiles of AHV using Nominal Dynamic Inversion . . . . .	20
3.3	Velocity Profiles $u, v, w$ in $x, y$ , and $z$ Directions Respectively using Nominal Dynamic Inversion . . . . .	21
3.4	Altitude ( $h$ ), Mass ( $M_v$ ) and Flight Path Angle ( $\gamma$ ) Profiles of AHV using Nominal Dynamic Inversion . . . . .	22
3.5	Roll Angle ( $\phi$ ), Pitch Angle ( $\theta$ ), and Yaw Angle ( $\psi$ ) Profiles of AHV using Nominal Dynamic Inversion . . . . .	22
3.6	Roll Rate ( $P$ ), Pitch Rate ( $Q$ ), and Yaw Rate ( $R$ ) Profiles of AHV using Nominal Dynamic Inversion . . . . .	23
3.7	Control Profiles using Nominal Dynamic Inversion . . . . .	23
3.8	Mach Number ( $M$ ), Angle of Attack ( $\alpha$ ) and Sideslip Angle ( $\beta$ ) Profiles for Different Initial Conditions using Nominal Dynamic Inversion . . . . .	24
3.9	Velocity Profiles $u, v, w$ in $x, y$ , and $z$ Directions Respectively for Different Initial Conditions using Nominal Dynamic Inversion . . . . .	25
3.10	Altitude ( $h$ ), Mass ( $M_v$ ) and Flight Path Angle ( $\gamma$ ) Profiles for Different Initial Conditions using Nominal Dynamic Inversion . . . . .	25
3.11	Roll Angle ( $\phi$ ), Pitch Angle ( $\theta$ ), and Yaw Angle ( $\psi$ ) Profiles for Different Initial Conditions using Nominal Dynamic Inversion . . . . .	26



3.12 Roll Rate ( $P$ ), Pitch Rate ( $Q$ ), and Yaw Rate ( $R$ ) Profiles for Different Initial Conditions using Nominal Dynamic Inversion . . . . .	26
3.13 Control Profiles for Different Initial Conditions using Nominal Dynamic Inversion	27
4.1 Mach Number ( $M$ ), Angle of Attack ( $\alpha$ ) and Sideslip Angle ( $\beta$ ) Profiles of AHV using Neuro-adaptive Dynamic Inversion . . . . .	33
4.2 Altitude ( $h$ ), Mass ( $M_v$ ) and Flight Path Angle ( $\gamma$ ) Profiles of AHV using Neuro-adaptive Dynamic Inversion . . . . .	34
4.3 Roll Angle ( $\phi$ ), Pitch Angle ( $\theta$ ), and Yaw Angle ( $\psi$ ) Profiles of AHV using Neuro-adaptive Dynamic Inversion . . . . .	34
4.4 Roll Rate ( $P$ ), Pitch Rate ( $Q$ ), and Yaw Rate ( $R$ ) Profiles of AHV using Neuro-adaptive Dynamic Inversion . . . . .	35
4.5 Control Profiles obtained using Neuro-adaptive Dynamic Inversion . . . . .	35
4.6 Mach Number ( $M$ ), Angle of Attack ( $\alpha$ ) and Sideslip Angle ( $\beta$ ) Profiles for Random Disturbances using Neuro-adaptive Dynamic Inversion . . . . .	36
4.7 Altitude ( $h$ ), Mass ( $M_v$ ) and Flight Path Angle ( $\gamma$ ) Profiles for Random Disturbances using Neuro-adaptive Dynamic Inversion . . . . .	37
4.8 Roll Angle ( $\phi$ ), Pitch Angle ( $\theta$ ), and Yaw Angle ( $\psi$ ) Profiles for Random Disturbances using Neuro-adaptive Dynamic Inversion . . . . .	37
4.9 Roll Rate ( $P$ ), Pitch Rate ( $Q$ ), and Yaw Rate ( $R$ ) Profiles for Random Disturbances using Neuro-adaptive Dynamic Inversion . . . . .	38
4.10 Control Profiles obtained for Random Disturbances using Neuro-adaptive Dynamic Inversion . . . . .	38
5.1 Mach Number ( $M$ ), Angle of Attack ( $\alpha$ ) and Sideslip Angle ( $\beta$ ) Profiles of AHV using Neuro-adaptive Generalized Dynamic Inversion . . . . .	45
5.2 Altitude ( $h$ ), Mass ( $M_v$ ) and Flight Path Angle ( $\gamma$ ) Profiles of AHV using Neuro-adaptive Generalized Dynamic Inversion . . . . .	46
5.3 Roll Angle ( $\phi$ ), Pitch Angle ( $\theta$ ), and Yaw Angle ( $\psi$ ) Profiles of AHV using Neuro-adaptive Generalized Dynamic Inversion . . . . .	46
5.4 Roll Rate ( $P$ ), Pitch Rate ( $Q$ ), and Yaw Rate ( $R$ ) Profiles of AHV using Neuro-adaptive Generalized Dynamic Inversion . . . . .	47

5.5	Control Profiles obtained using Neuro-adaptive Generalized Dynamic Inversion	47
5.6	Mach Number ( $M$ ), Angle of Attack ( $\alpha$ ) and Sideslip Angle ( $\beta$ ) Profiles for Random Disturbances using Neuro-adaptive Generalized Dynamic Inversion . . . . .	48
5.7	Altitude ( $h$ ), Mass ( $M_v$ ) and Flight Path Angle ( $\gamma$ ) Profiles for Random Disturbances using Neuro-adaptive Generalized Dynamic Inversion . . . . .	49
5.8	Roll Angle ( $\phi$ ), Pitch Angle ( $\theta$ ), and Yaw Angle ( $\psi$ ) Profiles for Random Disturbances using Neuro-adaptive Generalized Dynamic Inversion . . . . .	49
5.9	Roll Rate ( $P$ ), Pitch Rate ( $Q$ ), and Yaw Rate ( $R$ ) Profiles for Random Disturbances using Neuro-adaptive Generalized Dynamic Inversion . . . . .	50
5.10	Control Profiles obtained for Random Disturbances using Neuro-adaptive Generalized Dynamic Inversion . . . . .	50



## List of Tables

2.1	Important AHV Constants Used in Controller Design . . . . .	8
5.1	Quantitative Comparison Between Neuro-adaptive DI and GDI . . . . .	51

# 1 Introduction

## 1.1 Motivation

Air-breathing hypersonic vehicles (AHV) offer distinct performance advantages over rocket-based systems for space access vehicles. The major advantage of using air-breathing engine is that the extra oxidizer is not required for propulsion (rather oxygen from the atmosphere is used as the oxidizer). Moreover, there are no moving parts in the engine such as compressors and turbines, Hence, the propulsive system is easily integrated with the vehicle. Further, the speed of the hypersonic vehicle is very high (more than five times of sound speed), therefore, it takes very less time to reach the target/destination. However, these performance advantages are dependent upon advances in current state-of-the-art technologies in many critical areas, one of which happens to be the control system design.

The control and stabilization of AHV are very challenging because its aerodynamic characteristics are different from the conventional (subsonic or supersonic) air vehicles. Moreover, High velocity of AHV results into highly sensitive flight conditions which result in instability. This instability occurs mainly due to the constant center of pressure position irrespective of the angle of attack and altitude. The high velocity of the vehicle also results in weakly damped transient oscillations of the airframe [Coleman and Faruqi, 2009].

Furthermore, the engine performance of hypersonic vehicles is quite sensitive to the angle of attack and the sideslip angle. Deviation of these angles can even lead to the disastrous

condition of engine unstart. Moreover, at hypersonic speed, the behavior of the vehicle is highly nonlinear and coupled [Schmidt, 1993]. The high temperature and boundary layer effect on control surfaces place constraint on control surface deflection limits. This restricted control deflection limit places a great difficulty to a controller designer. This may lead to quick control saturation as well as less aerodynamic damping, leading to additional difficulties for control design [McRuer, 1991, Fidan et al., 2003]. Furthermore, hypersonic speeds cause the so-called “path-attitude decoupling” phenomenon, which is the resistance of the high momentum of the hypersonic vehicle to the change in the desired flight path [Mirmirani et al., 2005b]. Hence, the actual flight path gets fairly decoupled from the pitch attitude at hypersonic speeds.

Furthermore, Static stability margins decrease as the Mach number increases in AHV. Hence, in order to have reasonable static margins at hypersonic speeds, one needs to accept high-static stability margins [Mirmirani et al., 2005b]. Moreover, the stability of the AHV can not be defined only using static margin because of changes in center of gravity position (due to fuel burn-off). Hence, the active control augmentation is required to ensure the stability of the vehicle. The controller design problem is further complicated because of the fact that hypersonic aerodynamic parameters, as predicted from ground tests or theoretical computational methods, do not reflect the actual flight parameters. Further, another difficulty is the unavailability of a high fidelity dynamic model for hypersonic vehicles. This is largely because of the inherent difficulties of aerodynamic modeling in hypersonic flight regime as well as the lack of the sufficient number of flight tests (limited flight tests, that have been carried out, are all of the short duration and within a very restricted flight envelope as well) [Duan and Li, 2012, Mirmirani et al., 2005a]. These uncertainties in aerodynamic parameters require a control system design based on robust adaptive control techniques that learn the uncertainty on the data and provide a controller that is able to maintain desirable flight performance of AHV.

Hence, in this report, two kinds of robust adaptive control design approaches are presented for the stabilization of AHV in cruise phase. In the first approach, DI technique is used to derive the controller. Further, in second technique, Barrier Lyapunov function is used to derive the SC-GDI technique. In AHV, the angle of attack and sideslip angle need to be

regulated very tightly with limited control surface deflection to prevent inlet unstart and subsequently vehicle loss. Hence, both control techniques are augmented with newly developed constrained neuro-adaptive technique to learn the unknown disturbance function as well as its Jacobian matrix very quickly. Moreover, BLF is used to formulate constrained weight update law for unknown disturbance function learning. The effectiveness of the derived controllers are shown by promising simulation results.

## 1.2 Literature Survey

Air-breathing hypersonic vehicle (AHV) research gain a lot of attention from the researchers because of its explicit advantages over conventional air vehicles. Many researchers proposed various models of AHV and shown the effectiveness of the control algorithm. Since the AHV model is highly uncertain and nonlinear, hence, robust adaptive nonlinear controllers are preferred over linear controllers for controlling of AHV.

Longitudinal Winged-cone hypersonic model is used by [Marrison and Stengel \[1998\]](#) to design a robust control by assuming parameter uncertainties. [Marrison and Stengel \[1998\]](#) used the genetic algorithm to find unknown parameter values by selecting stochastic cost function. Further, a combination of dynamic inversion and the stochastic cost function is selected with the genetic algorithm by [Wang and Stengel \[2000\]](#) to design a robust controller. The robust adaptive controller is proposed by [\[Xu et al., 2012\]](#) with the application of neural network to control the longitudinal winged-cone hypersonic model.

Another longitudinal hypersonic vehicle model is developed by [Bolender and Doman \[2005\]](#) using hypersonic piston theory. Further, various practically useful variants of this model are proposed in the literature. Hypersonic vehicle dynamics during inlet unstart is investigated by [Bolender et al. \[2009\]](#) using CFD. Further, nonlinear dynamic inversion controller design for a non-minimum phase hypersonic vehicle is derived by [Kuipers et al. \[2008\]](#). Moreover, integrated guidance and control for longitudinal dynamics of the vehicle is shown by [Serrani et al. \[2009\]](#). The adaptive controller is proposed by [Gibson and Annaswamy \[2008\]](#) in presence of thrust and actuator uncertainties.

The third type of hypersonic longitudinal model is developed and verified by [Mirmi-](#)

rani et al. [2005a]. Further, aero-propulsive coupled analysis is shown by Clark et al. [2006]. Moreover, Time-varying vehicle model analysis and flexible mode analysis of the vehicle is presented by Fidan et al. [2006]. Further, Butt et al. [2010], Xu and Zhang [2015] formulated robust adaptive backstepping control methods for uncertain AHV.

The winged-cone model of an air-breathing hypersonic vehicle is developed by NASA for the analysis of six degree-of-freedom (six-DOF) motion of equations. Shaughnessy et al. [1990] estimated force and moment coefficients using hypersonic local surface inclination code and obtained as the discrete data point. Further, these aerodynamic coefficients are plotted as a function of Mach number, the angle of attack and control surface deflections. Moreover, the variation of Inertial components is also shown wrt. the center of gravity and mass of the vehicle. Further, [Keshmiri et al., 2005, 2004] used the plots of discrete data points (given by Shaughnessy et al. [1990]) and obtained the expressions of aerodynamic coefficients using higher order interpolation. Furthermore, the expressions of aero-coefficients are validated by CFD analysis [Keshmiri et al., 2006]. Six-DOF motion of equations for AHV are derived by Keshmiri et al. [2007] and further enhanced to ten degree-of-freedom motion of equations [Colgren et al., 2009]. An adaptive inverse controller for AHV is proposed by Qian and Jiaxue [2010] with the help of the neural network.

Other six-DOF model of AHV are presented by Vick [2014], Chamitoff [1992]. The adaptive robust controller is derived by Rollins et al. [2013], using dynamic inversion technique for the model proposed by Vick [2014]. Further, the same model is used by Famularo et al. [2016] to obtain a state-constrained control solution for AHV using projection operator. Control-oriented modeling of AHV is done by Huifeng et al. [2011] using parameterized configuration approach.

feedback linearization concept of control design is presented by Isidori [2013] for various class of nonlinear systems. In this method, the nonlinear system is transformed in a way such that it appeared linear in transformed coordinates. Further, using stable linear error dynamics, dynamic inversion control technique is derived by Slotine et al. [1991]. However, this control design technique assumed that the system is perfectly known, which is very rare. Hence, to overcome this limitation, Padhi et al. [2007] presented a neuro-adaptive dynamic inversion

approach for robust control design, in which the bounded disturbance function is learned by the controller over time. Further, Ambati and Padhi [2016] augmented neuro-adaptive control design technique with jacobian matrix learning of unknown disturbance function to minimize the transients.

Furthermore, Tee et al. [2009] formulated the output constraint nonlinear control for strict-feedback SISO nonlinear system by selecting barrier Lyapunov function (BLF) as a Lyapunov candidate. BLF is obtained by constraining the radially unbounded quadratic Lyapunov function (QLF) into a locally bounded region. Moreover, backstepping control design technique used by Tee et al. [2009] to obtain output constraint control for both known and uncertain SISO nonlinear systems. Output constrained control design technique is further enhanced by selecting time varying bound for uncertain SISO nonlinear system by Tee and Ge [2011].

### 1.3 Control Objectives

The main control objective in this report is to design a robust adaptive control algorithm that stabilizes the AHV during the cruise flight and prevent inlet unstart. Moreover, the controller should be robust enough to take care of model uncertainties and disturbance, hence, additional controller design objective is to minimize the need of high fidelity AHV model. The mission scenario is shown in Fig. 1.1, where, the AHV is required to follow the desired path without much deviation. Therefore, further, control objectives are to maintain the states as well as the error in disturbance learning within the prefixed desired bounds.



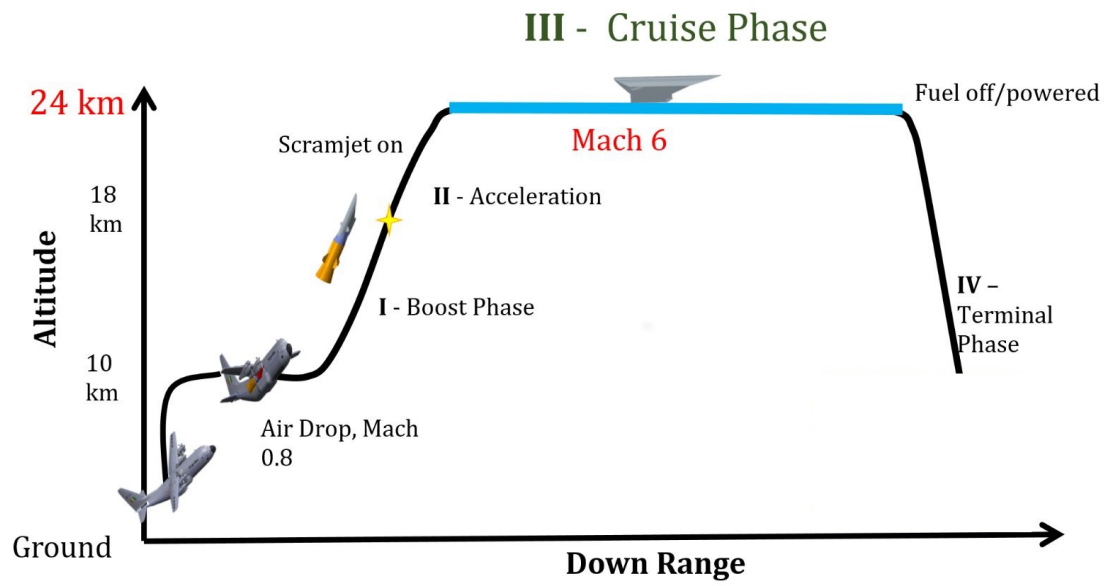


Figure 1.1 – Mission Scenario

## 2 Hypersonic Vehicle Model Selection and Vehicle Dynamics

### 2.1 Vehicle Dynamics

Rigid winged-cone model of air-breathing hypersonic vehicle (AHV) is selected in this report to derive the robust adaptive controller. The AHV geometry is shown in Fig. 2.1, in which propulsive system is integrated with the vehicle. The selected vehicle model is having canard configuration, however, the canard is used only for subsonic/supersonic speed regime. As the AHV speed approached to hypersonic speed, the canard fins are closed inside the vehicle frame, hence, canards have no effect in hypersonic flight.

The vehicle dimension and parameter values, obtained by [Shaughnessy et al. \[1990\]](#), are given in foot-pound-second unit system, therefore, first values are converted into meter-kilogram-second unit system. The aerodynamic coefficients, presented by [Keshmiri et al. \[2005\]](#), are dimension less hence, there is no need to maintain dimension compatibility. Further, the important vehicle related constants used in controller design and analysis are summarized in Table 2.1

The vehicle configuration shown in Fig. 2.1 is assumed to have the thrust vector orientation perfectly aligned with body  $x$  axis. Hence, there is no thrust force component in body  $y$  and  $z$  directions.

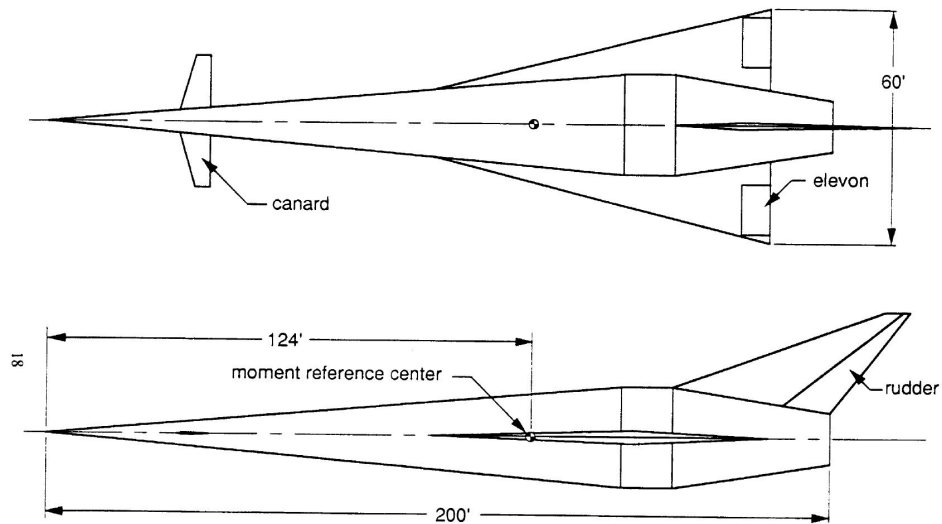


Figure 2.1 – Air-breathing Hypersonic Vehicle Geometry [Shaughnessy et al., 1990]

Table 2.1 – Important AHV Constants Used in Controller Design

AHV Constants	Value
Mass ( $M_v$ )	136080 kg
Wing Reference Area ( $S$ )	334.7295 m <sup>2</sup>
Wing Span ( $b$ )	18.2880 m
Mean Aerodynamics Chord ( $c$ )	24.384 m
Moment Reference Center ( $x_{mrc}$ )	37.7952 m
Gravity ( $g$ )	9.8 $\frac{m}{sec^2}$
Maximum Thrust ( $T_{max}$ )	1467900 N
Specific Impulse ( $I_{sp}$ )	1000 g sec

The translational dynamic equations of AHV are given as

$$\begin{aligned}
 \dot{u} &= Rv - Qw - g \sin \theta + \frac{F_{ax} + F_{Tx}}{M_v} \\
 \dot{v} &= wP - vR + g \cos \theta + \frac{F_{ay}}{M_v} \\
 \dot{w} &= uQ - vP + g \cos \theta + \frac{F_{az}}{M_v}
 \end{aligned} \tag{2.1}$$

The translational dynamic equations (2.1) of AHV can also be transformed into  $\dot{V}_t$ ,  $\dot{\alpha}$ ,

and  $\dot{\beta}$  variables as

$$\begin{aligned}\dot{V}_t &= \frac{u\dot{u} + v\dot{v} + w\dot{w}}{V_t} \\ \dot{\alpha} &= \frac{u\dot{w} - w\dot{u}}{u^2 + w^2} \\ \dot{\beta} &= \frac{(\dot{v}V_t - v\dot{V}_t)\cos\beta}{u^2 + w^2}\end{aligned}\quad (2.2)$$

where, total AHV velocity ( $V_t$ ), angle of attack ( $\alpha$ ), and sideslip angle ( $\beta$ ) is calculated as

$$V_t = \sqrt{u^2 + v^2 + w^2}, \quad \alpha = \tan^{-1}\left(\frac{w}{u}\right), \quad \beta = \sin^{-1}\left(\frac{v}{V_t}\right)$$

The rotational dynamic equations of AHV are given as

$$\begin{aligned}\dot{P} &= c_1QR + c_2PQ + c_3L_{am} + c_4N_a \\ \dot{Q} &= c_5PR - c_6(P^2 - R^2) + c_7M_a \\ \dot{R} &= c_8PQ - c_2QR + c_4L_{am} + c_9N_a\end{aligned}\quad (2.3)$$

The rotational kinematic equations of AHV are given as

$$\begin{aligned}\dot{\phi} &= P + Q\sin\phi\tan\theta + R\cos\phi\tan\theta \\ \dot{\theta} &= Q\cos\phi - R\sin\phi \\ \dot{\psi} &= Q\sin\phi\sec\theta + R\cos\phi\sec\theta\end{aligned}\quad (2.4)$$

The translational kinematic equations of AHV are given as

$$\begin{aligned}\dot{x} &= u\cos\theta\cos\psi + (\sin\phi\sin\theta\cos\psi - \cos\phi\sin\psi)v + (\cos\phi\sin\theta\cos\psi + \sin\phi\sin\psi)w \\ \dot{y} &= u\cos\theta\sin\psi + (\sin\phi\sin\theta\sin\psi + \cos\phi\cos\psi)v + (\cos\phi\sin\theta\sin\psi - \sin\phi\cos\psi)w \\ \dot{h} &= u\sin\theta - v\sin\phi\cos\theta - w\cos\phi\cos\theta\end{aligned}\quad (2.5)$$

Here,  $u$ ,  $v$ , and  $w$  are the body velocities in  $x$ ,  $y$ , and  $z$  directions respectively. Further, roll, pitch and yaw angles are denoted as  $\phi$ ,  $\theta$  and  $\psi$ .  $P$ ,  $Q$  and  $R$  are roll rate, pitch rate and

yaw rate around body  $x$ ,  $y$ , and  $z$  axis respectively. Moreover,  $h$  is the altitude of the vehicle in inertial frame and  $x$  and  $y$  are the distances covered by AHV in inertial frame of reference.

Furthermore,  $F_{ax}$ ,  $F_{ay}$ , and  $F_{az}$  are the aerodynamic body forces acted in  $x$ ,  $y$ , and  $z$  directions respectively. Further,  $F_{T_x}$  is the thrust force along body  $x$  axis. Moreover,  $M_v$  is the mass of the AHV [Shaughnessy et al., 1990] and  $g$  is the gravity force acting on the vehicle in inertial frame of reference. The moments,  $L_{am}$ ,  $M_a$ , and  $N_a$  are the aerodynamic moments around center of gravity. Further, coefficients  $c_1, c_2, \dots, c_9$  are calculated from inertia values of the AHV and calculated as

$$\begin{bmatrix} c_1 \\ c_2 \\ c_3 \\ c_4 \\ c_8 \\ c_9 \end{bmatrix} = \frac{1}{(I_{xx}I_{zz} - I_{xz}^2)} \begin{bmatrix} I_{zz}(I_{yy} - I_{zz}) - I_{xz}^2 \\ I_{xz}(I_{zz} + I_{xx} - I_{yy}) \\ I_{zz} \\ I_{yz} \\ I_{xx}(I_{xx} - I_{yy}) + I_{xz}^2 \\ I_{xx} \end{bmatrix}$$

$$c_5 = (I_{zz} - I_{xx})/I_{yy}$$

$$c_6 = I_{xz}/I_{yy}$$

$$c_7 = 1/I_{yy}$$

The inertia values of AHV varies with respect to mass because mass consumption is assumed during flight. The expression for the inertia values are obtained by Zhang et al. [2010] and given as

$$\begin{aligned} I_{xx} &= -7.8809 \times 10^{-5} M_v^2 + 25.88576 M_v - 6.9683 \times 10^5 \\ I_{yy} &= -8.2890 \times 10^{-4} M_v^2 + 265.9889 M_v - 7.3048 \times 10^6 \\ I_{zz} &= I_{yy} \\ I_{xz} &= 0 \end{aligned}$$

where,  $I_{xx}, I_{yy}$ , and  $I_{zz}$  are diagonal terms of inertia matrix and  $I_{xz}$  is cross diagonal

term. Further, in AHV, the fuel consumption is very high, hence, the mass variation of AHV is considered while designing the controller. The mass variation dynamics is given as

$$\dot{M}_v = -\frac{\sigma_T T_{max}}{I_{sp}g} \quad (2.6)$$

where, new control variable  $\sigma_T$  is defined as  $\sigma_T = \frac{T}{T_{max}}$ . Here,  $T$  is the required thrust magnitude and  $T_{max}$  is the maximum thrust that AHV can generate [Keshmiri et al., 2004]. The specific impulse of thrust is denoted by  $I_{sp}$ . Further, the hypersonic speed generally expressed in term of mach number. Hence, the conversion from velocity to mach number is given as

$$M = \frac{V_t}{a} \quad (2.7)$$

where  $a$  is the speed of sound which is constant for cruise flight and  $V_t$  is the total velocity of the vehicle.

## 2.2 Forces and Moments Calculation

In this section, the calculation of forces and moments used in six degree-of-freedom dynamics of AHV are presented. The expressions for force and moment coefficients are obtained by Keshmiri et al. [2005] using higher order interpolation. Moreover, the obtained aerodynamic coefficient expressions are function of  $M$ ,  $\alpha$  (in degree) and control surface deflections (in degree). Further, the AHV consist of four controls  $\delta_e$ ,  $\delta_a$ ,  $\delta_r$  and  $\sigma_T$ . Among the four control variables,  $\delta_e$ ,  $\delta_a$ , and  $\delta_r$  are control surface deflection for right elevon, left elevon and rudder respectively and  $\sigma_T$  is used to maintain the thrust requirement to regulate the AHV speed.

The calculation of aerodynamic forces are done in the similar way as explained in [Shaughnessy et al., 1990] to maintain the compatibility. The drag force  $D$  is calculated as

$$D = \bar{q}SC_D \quad (2.8)$$

where,  $\bar{q}$  is the dynamic pressure obtained as  $\bar{q} = \frac{1}{2}\rho V_t^2$ ,  $V_t$  is total AHV velocity and  $\rho$  is the pressure. The surface area of the vehicle is denoted as  $S$ . The drag coefficient  $C_D$  is calculated as

$$C_D = C_{Da} + C_{D,\delta_e} + C_{D,\delta_a} + C_{D,\delta_r}$$

here,  $C_{Da}$  is the basic drag incremental coefficient and  $C_{D,\delta_e}$ ,  $C_{D,\delta_a}$  and  $C_{D,\delta_r}$  are drag incremental coefficients for right elevon, left elevon and rudder respectively.

Further, the Lift force  $L$  is calculated as

$$L = \bar{q}SC_L \quad (2.9)$$

where, the lift coefficient  $C_L$  is obtained as

$$C_L = C_{La} + C_{L,\delta_e} + C_{L,\delta_a} + C_{L,\delta_r}$$

here,  $C_{La}$  is the basic lift incremental coefficient and  $C_{L,\delta_e}$ ,  $C_{L,\delta_a}$  and  $C_{L,\delta_r}$  are lift incremental coefficients for right elevon, left elevon and rudder respectively.

The side force  $Y$  is calculated as

$$Y = \bar{q}SC_Y \quad (2.10)$$

where,  $C_Y$  is the side force coefficient, calculated as

$$C_Y = C_{Y\beta}\beta + C_{Y,\delta_e} + C_{Y,\delta_a} + C_{Y,\delta_r}$$

here,  $C_{Y\beta}$  is the basic vehicle sideslip derivative and  $\beta$  is known as sideslip angle which is in radians. Further,  $C_{Y,\delta_e}$ ,  $C_{Y,\delta_a}$  and  $C_{Y,\delta_r}$  are incremental coefficients for right elevon, left elevon and rudder respectively.

The rolling moment  $L_{Ac}$  is given as

$$L_{Ac} = \bar{q} S b C_{lm} \quad (2.11)$$

here,  $C_{lm}$  is the rolling moment coefficient, calculated as

$$C_{lm} = C_{l\beta} \beta + C_{l,\delta_e} + C_{l,\delta_a} + C_{l,\delta_r} + C_{l_p} \left( \frac{Pb}{2V} \right) + C_{l_r} \left( \frac{Rb}{2V} \right)$$

Here,  $C_{l\beta}$  is the basic rolling moment with sideslip derivative and  $C_{l,\delta_e}$ ,  $C_{l,\delta_a}$ ,  $C_{l,\delta_r}$  are rolling moment incremental coefficients for right elevon, left elevon and rudder respectively. Further,  $C_{l_p}$  and  $C_{l_r}$  are rolling moment derivative for roll rate and yaw rate.

The pitching moment  $M_{Ac}$  relative to moment reference center is calculated as

$$M_{Ac} = \bar{q} S c C_m \quad (2.12)$$

where,  $C_m$  is the pitching moment coefficient, obtained as

$$C_m = C_{ma} + C_{m,\delta_e} + C_{m,\delta_a} + C_{m,\delta_r} + C_{m_q} \left( \frac{Qc}{2V} \right)$$

Here,  $C_{ma}$  is the basic pitching moment incremental coefficient relative to moment reference center and  $C_{m,\delta_e}$ ,  $C_{m,\delta_a}$ ,  $C_{m,\delta_r}$  are pitching moment incremental coefficients for right elevon, left elevon and rudder respectively. Moreover,  $C_{m_q}$  is pitch rate dynamic derivative.

The yawing moment  $N_{Ac}$  relative to moment reference center is calculated as

$$N_{Ac} = \bar{q} S b C_n \quad (2.13)$$

where, yawing moment coefficient  $C_n$  is calculated as

$$C_n = C_{n\beta} \beta + C_{n,\delta_e} + C_{n,\delta_a} + C_{n,\delta_r} + C_{n_p} \left( \frac{Pb}{2V} \right) + C_{n_r} \left( \frac{Rb}{2V} \right)$$



Here,  $C_{n\beta}$  is the basic yawing moment with sideslip derivative and  $C_{l,\delta_e}$ ,  $C_{l,\delta_a}$ ,  $C_{l,\delta_r}$  are yawing moment incremental coefficients for right elevon, left elevon and rudder respectively. Further,  $C_{n_p}$  and  $C_{n_r}$  are yawing moment derivative for roll rate and yaw rate.

The aerodynamic and thrust forces used in six-DoF equations (2.1) are obtained as

$$\begin{aligned} F_{ax} &= L \sin \alpha - D \cos \alpha \\ F_{ay} &= Y \\ F_{az} &= -D \sin \alpha - L \cos \alpha \\ F_{Tx} &= \sigma T_{\max} \end{aligned}$$

The aerodynamic moments used in six-DoF equations (2.3) are calculated as

$$\begin{aligned} L_{am} &= L_{Ac} \\ M_a &= M_{Ac} - X_{cg} F_{az} \\ N_a &= N_{Ac} + X_{cg} F_{ay} \end{aligned}$$

here,  $L_{am}$ ,  $M_a$ , and  $N_a$  are the aerodynamic moments around center of gravity. Moreover,  $L_{Ac}$ ,  $M_{Ac}$ , and  $N_{Ac}$  are the aerodynamic moments around moment reference center of vehicle. Further, the mass of the AHV varies with time, hence, center of gravity  $X_{cg}$  also varies with time. The expression of  $X_{cg}$  (in meter) wrt. mass is given as (Zhang et al. [2010])

$$X_{cg} = 1.6210 \times 10^{-10} M_v^2 - 5.5226 \times 10^{-5} M_v + 7.3578 \quad (2.14)$$

## 3 Nominal Dynamic Inversion Control

### Design of Hypersonic Vehicle

In this section, three-loop-control design architecture is presented for the air-breathing hypersonic vehicle (AHV) as shown in Fig. 3.1. Dynamic inversion technique is used to obtain the controller for tracking the reference signal. Three-loop-control design consist of three loops, the outer loop is used to obtain the desired pitch angle  $\theta^*$ . Further, the desired pitch angle  $\theta^*$  is the angle required to track the constant altitude. Furthermore, the output of the outer loop is used as the reference command for the intermediate loop. Hence, by using DI, the desired roll rate  $P^*$ , pitch rate  $Q^*$ , and yaw rate  $R^*$  are obtained to track the reference input. Finally, in the inner loop, the control surfaces deflection is calculated to track the desired angular rates obtained from the intermediate loop. Further, the velocity controller is used to maintain the desired velocity of the vehicle to prevent the inlet unstart (low vehicle speed is also a reason of inlet unstart). Further, velocity controller is used to obtain the required amount of thrust, that is needed to maintain the desired velocity of the AHV. The dynamic inversion (DI) formulation of all three loops is given in further sections

#### 3.1 Outer Loop Control design

The controller is designed for cruise phase of the flight, hence, the constant altitude is reference signal to the outer loop. Dynamic inversion is used to obtained the desired pitch angle  $\theta^*$  from  $\dot{h}$  equation (2.5). Further, the the derivative of the desired reference signal is assumed to

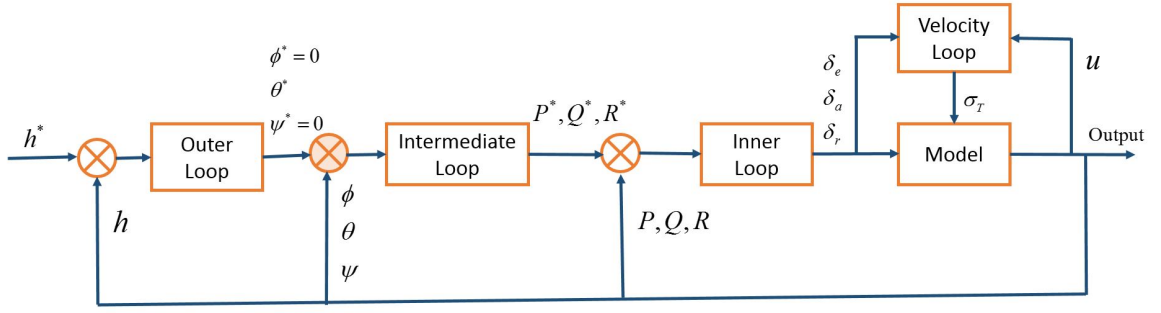


Figure 3.1 – Block Diagram of Three-Loop-Control Design

be zero. Hence, using dynamic inversion, the error dynamics is written as

$$\dot{e}_h + k_h e_h = 0$$

here  $e_h = h^* - h$  is the error in reference height and obtained height and  $k_h$  is positive constant gain. Further, the error dynamics is expended as

$$\begin{aligned} (\dot{h}^* - \dot{h}) + k_h(h^* - h) &= 0 \\ \dot{h} &= k_h(h^* - h) \end{aligned}$$

Using  $\dot{h}$  equation from equation 2.5, the error dynamics can be rewritten as

$$u \sin \theta - (v \sin \phi + w \cos \phi) \cos \theta = k_h(h^* - h)$$

On solving for pitch angle ( $\theta = \theta^*$ ) and rearranging the terms, the desired pitch angle  $\theta^*$  is obtained as

$$\theta^* = \tan^{-1} \left( \frac{v \sin \phi + w \cos \phi}{u} \right) - \sin^{-1} \left( \frac{k_h(h^* - h)}{\sqrt{u^2 + [v \sin \phi + w \cos \phi]^2}} \right) \quad (3.1)$$

Furthermore, desired roll angle  $\phi^*$  and desired yaw angle  $\psi^*$  is assumed to be zero as reference values for intermediate loop.

### 3.2 Intermediate Loop Control design

The output of the outer loop is act as the reference signals for the intermediate loop. The desired roll rate  $P^*$ , pitch rate  $Q^*$ , and yaw rate  $R^*$  are obtained by using DI. The error dynamics of the intermediate loop is written as

$$\begin{bmatrix} \dot{e}_\phi \\ \dot{e}_\theta \\ \dot{e}_\psi \end{bmatrix} + \begin{bmatrix} k_\phi & 0 & 0 \\ 0 & k_\theta & 0 \\ 0 & 0 & k_\psi \end{bmatrix} \begin{bmatrix} e_\phi \\ e_\theta \\ e_\psi \end{bmatrix} = 0$$

Here,  $e_\phi = \phi^* - \phi$ , is the error between the desired roll angle and obtained roll angle. Similarly,  $e_\theta = \theta^* - \theta$ , is the error between desired and obtained pitch angle and  $e_\psi = \psi^* - \psi$ , is the error between desired and obtained yaw angle. Moreover,  $k_\phi$ ,  $k_\theta$  and  $k_\psi$  are positive definite constants. Further, rearranging the intermediate loop error dynamics using equations 2.4, the desired body rates are obtained as

$$\begin{bmatrix} P^* \\ Q^* \\ R^* \end{bmatrix} = \begin{bmatrix} 1 & \tan\theta \sin\phi & \tan\theta \cos\phi \\ 0 & \cos\phi & -\sin\phi \\ 0 & \sin\phi \sec\theta & \cos\phi \sec\theta \end{bmatrix}^{-1} \begin{bmatrix} k_\phi (\phi^* - \phi) \\ k_\theta (\theta^* - \theta) \\ k_\psi (\psi^* - \psi) \end{bmatrix}$$

### 3.3 Inner Loop Control design

In this section, the control surfaces deflection are obtained as an output using DI on the inner loop. In the inner loop, the desired body rates obtained from intermediate loop are considered as reference signals and equations 2.3 are used to formulate the error dynamics. Further, the inner loop error dynamics is written as

$$\begin{bmatrix} \dot{e}_P \\ \dot{e}_Q \\ \dot{e}_R \end{bmatrix} + \begin{bmatrix} k_P & 0 & 0 \\ 0 & k_Q & 0 \\ 0 & 0 & k_R \end{bmatrix} \begin{bmatrix} e_P \\ e_Q \\ e_R \end{bmatrix} = 0$$

Here,  $e_P = P^* - P$ , is the error between the desired roll rate and obtained roll rate. Similarly,  $e_Q = Q^* - Q$ , is the error between desired and obtained pitch rate and  $e_R = R^* - R$  is the error between desired and obtained yaw rate. Moreover,  $k_P$ ,  $k_Q$  and  $k_R$  are positive definite constants. Further, rearranging the error dynamics using equations 2.3, the following nonlinear coupled equations are obtained as

$$\begin{aligned} k_P(P - P^*) + c_3 L_{am} &= 0 \\ c_5 P R + k_Q(Q - Q^*) + c_7 M_a &= 0 \\ c_8 P Q + k_R(R - R^*) + c_9 N_a &= 0 \end{aligned}$$

The above equations contained only control surface deflections  $\delta_e$ ,  $\delta_a$ , and  $\delta_r$  as an unknown. Hence, Newton-Raphson algorithm is used to obtain the desired control surface deflections.

### 3.4 Velocity Loop Control design

Velocity control loop is an extra loop presented in the control design to maintain the constant desired velocity of the AHV. The forward velocity  $u$  is the major component of the AHV velocity and other velocity components are negligible as compared to forward velocity. Hence, dynamic inversion technique is used on forward velocity equation given in equation 2.1 to obtained the desired thrust magnitude for maintaining the desired velocity. The velocity loop error dynamics is written as

$$\dot{e}_u + k_u e_u = 0$$

here  $e_u = u^* - u$ , is the error between the desired forward velocity and obtained forward velocity and  $k_u$  is positive constant gain. Further, the error dynamics is expended as

$$\dot{u} = k_u(u^* - u)$$

Further, the desired  $\sigma_T$  is obtained using equation 2.1 as

$$\sigma_T = \left( \frac{M_v}{T_{max}} \right) \left[ - \left( vR - QW - g \sin \theta + \frac{F_{ax}}{M_v} \right) + k_u(u^* - u) \right] \quad (3.2)$$

### 3.5 Simulation Results

#### 3.5.1 Calculation of Trim Conditions

Trim conditions needed to be calculated before carrying out the simulations. Trim conditions are the conditions around which the aircraft is in equilibrium. To obtain trim conditions for the cruise flight, the constant height and constant forward velocity are assumed as  $h^* = 24000 \text{ m}$  and  $u^* = 1786.4 \text{ m/s}$ . Accordingly,  $P$ ,  $Q$ ,  $R$  and  $\phi$  is assumed as zero. Further, the variables  $[v, w, \theta, \delta_e, \delta_a, \delta_r, \sigma_T]^T$  can be calculated from the equations  $[\dot{u}, \dot{v}, \dot{w}, \dot{P}, \dot{Q}, \dot{R}, \dot{h}]^T = 0$  using Newton-Raphson method. Further,  $\psi$ ,  $x$  and  $y$  are not appeared in any of the equations used for trim calculation, hence  $\dot{\psi}$ ,  $\dot{x}$  and  $\dot{y}$  equations are not included in trim calculation. Finally, the trim conditions are obtained as  $v = 0 \text{ m/s}$ ,  $w = 91.8 \text{ m/s}$ ,  $\theta = 2.94^\circ$ ,  $\delta_e = -7.21^\circ$ ,  $\delta_a = -7.21^\circ$ ,  $\delta_r = 0^\circ$ ,  $\sigma_T = 0.194$ .

#### 3.5.2 Simulation results

In this section, the results obtained from the nominal controller is presented. The results are obtained by varying the initial conditions around the trim values to show the applicability of the obtained controller. For simulations,  $rk^4$  method is used with step size as  $0.01 \text{ sec}$ . The results are simulated for  $150 \text{ sec}$ . All the vehicle parameter and force-moment coefficients are taken from the literature published by [Shaughnessy et al., 1990] and Keshmiri et al. [2005].

The initial conditions around the trim values are given as,  $u = 1836.4 \text{ m/s}$ ,  $v = 0 \text{ m/s}$ ,  $w = 91.8 \text{ m/s}$ ,  $P = 3 \text{ deg/sec}$ ,  $Q = 2 \text{ deg/sec}$ ,  $R = -3 \text{ deg/sec}$ ,  $\phi = 0 \text{ deg}$ ,  $\theta = 2.94 \text{ deg}$ ,  $\psi = 0 \text{ deg}$ ,  $x = 0 \text{ m}$ ,  $y = 0 \text{ m}$ ,  $h = 24100 \text{ m}$  and initial mass  $M_v = 136077.6 \text{ kg}$ . The inner loop gains  $k_P$ ,  $k_Q$ , and  $k_R$  are selected as 2.0 and the intermediate loop gains  $k_\phi$ ,  $k_\theta$ , and  $k_\psi$  are selected as 0.2. Further the outer loop control gain  $k_h$  is selected as 0.01 and the velocity loop controller gain is chosen as 0.01.

The velocity, angle of attack and sideslip angle profiles are shown in Fig. 3.2 respectively. Velocity is perfectly tracked by the application of derived nominal controller. The angle of attack is within the bound to prevent the inlet unstart. Further, sideslip angle is zero after sometimes hence the reference trajectory is effectively tracked by the AHV.

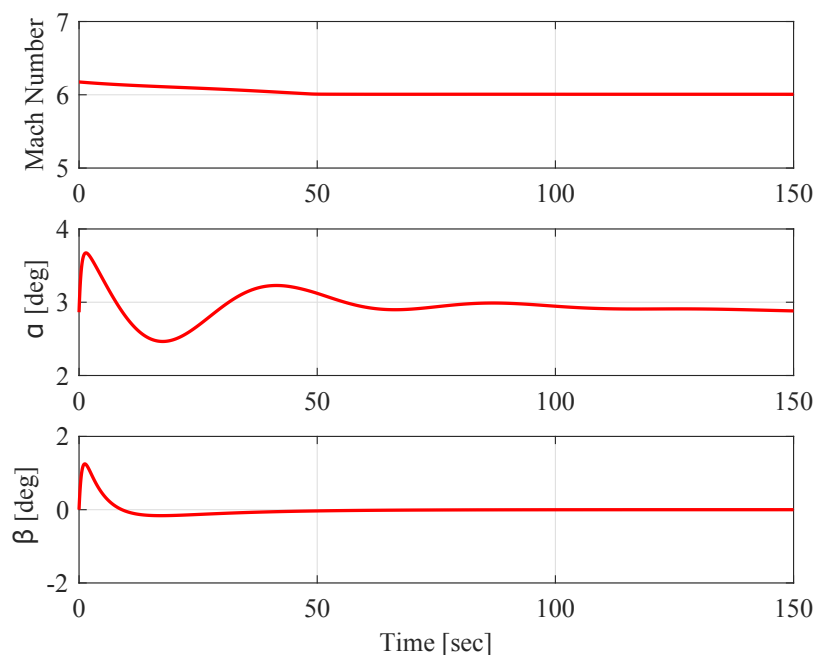


Figure 3.2 – Mach Number ( $M$ ), Angle of Attack ( $\alpha$ ) and Sideslip Angle ( $\beta$ ) Profiles of AHV using Nominal Dynamic Inversion

Further, the profiles of components of the velocity are shown in Fig. 3.3 respectively. The forward velocity  $u$  is the major component of velocity and become constant after a finite time, hence the required velocity is maintained by the AHV to prevent inlet unstart. Further, the cross velocity  $v$  become zero, hence there is side deviation. Furthermore, the altitude profile is shown in Fig. 3.4. The reference altitude is nearly tracked by the states, however, tracking altitude is not a major concern here, hence, the results are acceptable. The continuous and smooth mass and flight path angle profiles of the AVH are shown in Fig. 3.4. The flight path angle is become zero after finite time, which means the AHV is flying at zero angle wrt. inertial frame of reference.

Roll, pitch, and yaw angle profiles are presented in Fig. 3.5. The roll and yaw angle profiles are perfectly tracking zero in spite of the variation in initial conditions hence, the AHV is stabilized after the control application (AHV is inherently unstable). Further, the pitch angle profile is stabilized at a non-zero value, which is essential to generate the necessary lift in the AHV.

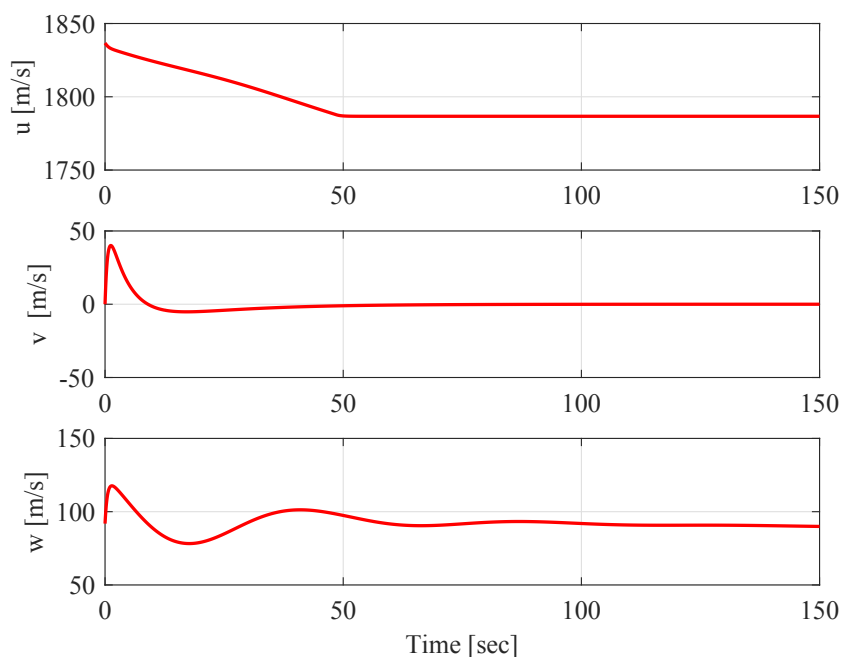


Figure 3.3 – Velocity Profiles  $u, v, w$  in  $x, y$ , and  $z$  Directions Respectively using Nominal Dynamic Inversion

The angular rate profiles are shown in Fig. 3.6 respectively. After some transients, the angular rate profiles are stabilized at zero, which means AHV reached the equilibrium point. Hence, the controller formulated using nominal DI is effective for control and stabilization of AHV. Furthermore, the stabilization time for inner loop variables is lesser than the intermediate loop variables because of the three-loop-control design methodology. The control profiles are shown in Fig. 3.7. The control surface deflections are within the saturation limits  $[-40^\circ, 30^\circ]$  hence, the solution provided by the controller is physically realizable. Further, the control  $\sigma_T$  is saturated within the bound  $[0.1, 0.9]$ , hence, the velocity profile takes times to track the desired trajectory. However, the stability of the vehicle is ensured by the derived nominal controller.



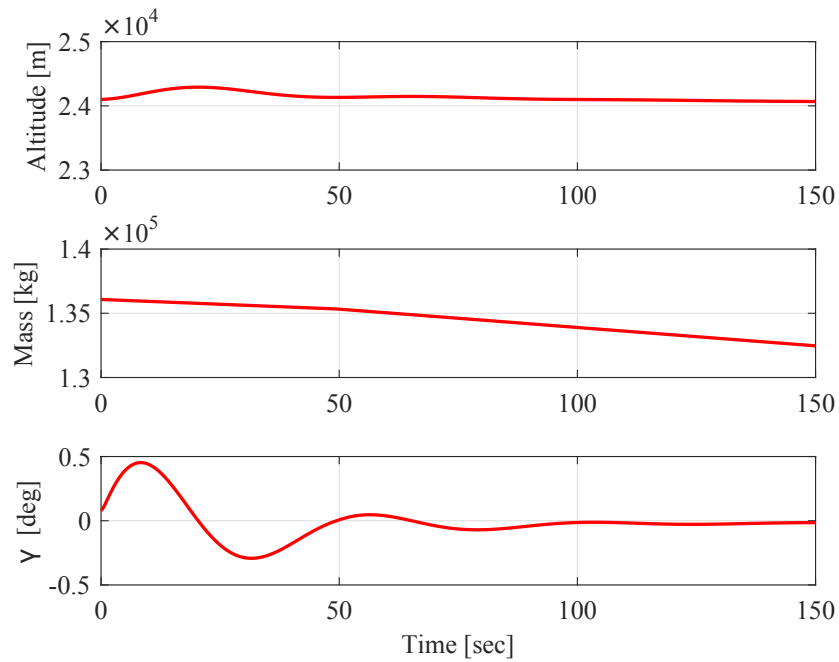


Figure 3.4 – Altitude ( $h$ ), Mass ( $M_v$ ) and Flight Path Angle ( $\gamma$ ) Profiles of AHV using Nominal Dynamic Inversion

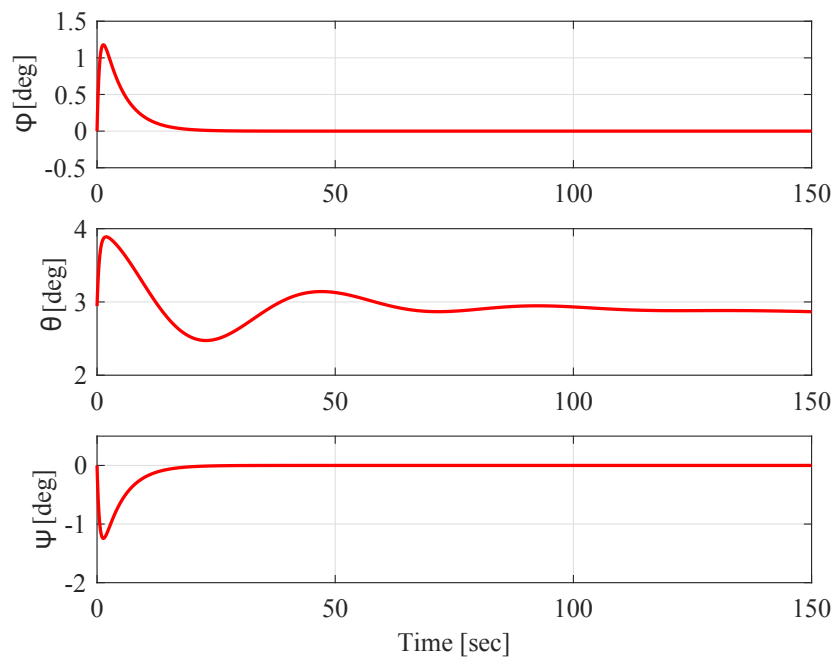


Figure 3.5 – Roll Angle ( $\phi$ ), Pitch Angle ( $\theta$ ), and Yaw Angle ( $\psi$ ) Profiles of AHV using Nominal Dynamic Inversion

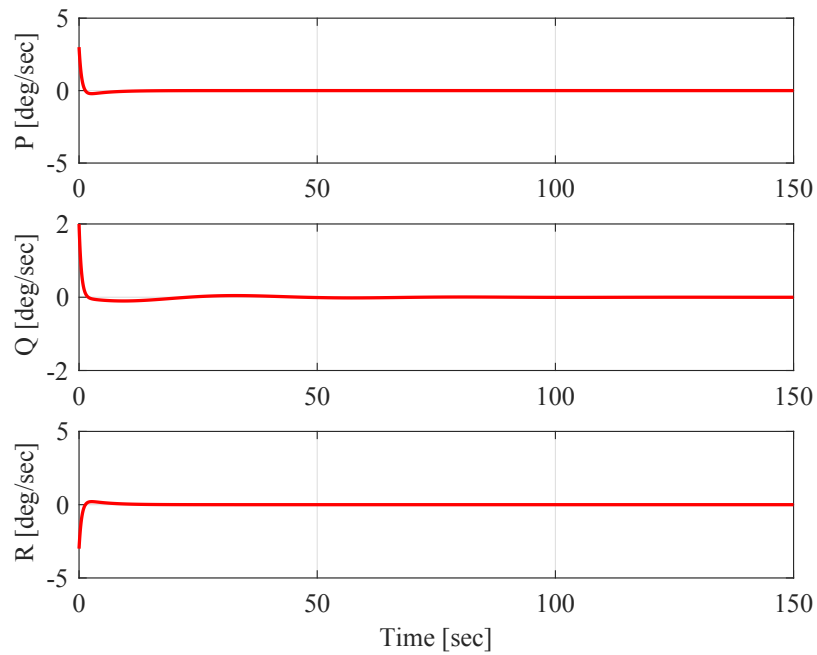


Figure 3.6 – Roll Rate ( $P$ ), Pitch Rate ( $Q$ ), and Yaw Rate ( $R$ ) Profiles of AHV using Nominal Dynamic Inversion

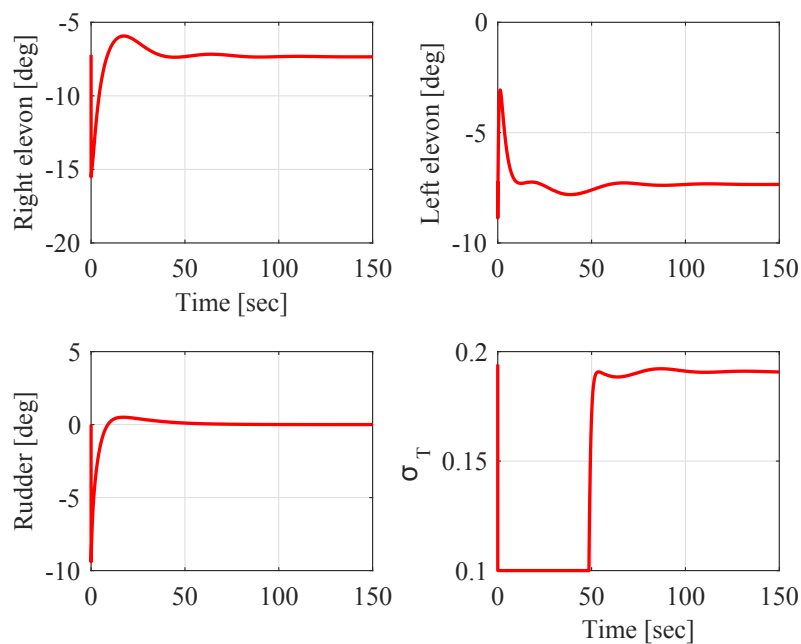


Figure 3.7 – Control Profiles using Nominal Dynamic Inversion

Further, the simulation results are presented for various different initial conditions around trim values to show the effectiveness of the nominal DI controller. The random perturbation in forward velocity  $u$  is assumed in between  $[-100, 100]$   $m/s$  around trim value. Moreover, the initial condition random perturbation in angular rates are assumed in between  $[-5, 5]$   $deg/sec$  around trim values. Further, the random perturbation in altitude is assumed in between  $[-500, 500]$   $m$  around trim value.

Velocity, angle of attack and sideslip angle profiles are shown in Fig. 3.8 and Fig. 3.9 for various initial conditions. The velocity profiles for each initial condition follow the same trend and become constant after some time. Similarly, the angle of attack profiles are also within the accepted range to prevent inlet unstart. Further, the altitude profiles are shown in Fig. 3.10 for various initial conditions. All the altitude profiles are converged around the reference value. Furthermore, mass and flight path angle profiles are shown in Fig. 3.10 for perturbed initial conditions. The flight path angle profiles are converged to zero within the finite time, which shown the effectiveness of the derived controller.

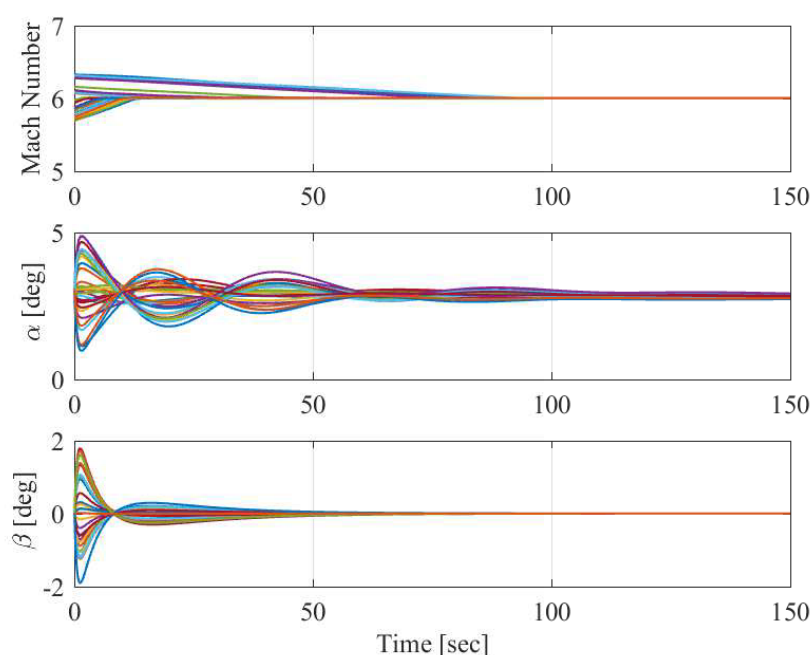


Figure 3.8 – Mach Number ( $M$ ), Angle of Attack ( $\alpha$ ) and Sideslip Angle ( $\beta$ ) Profiles for Different Initial Conditions using Nominal Dynamic Inversion

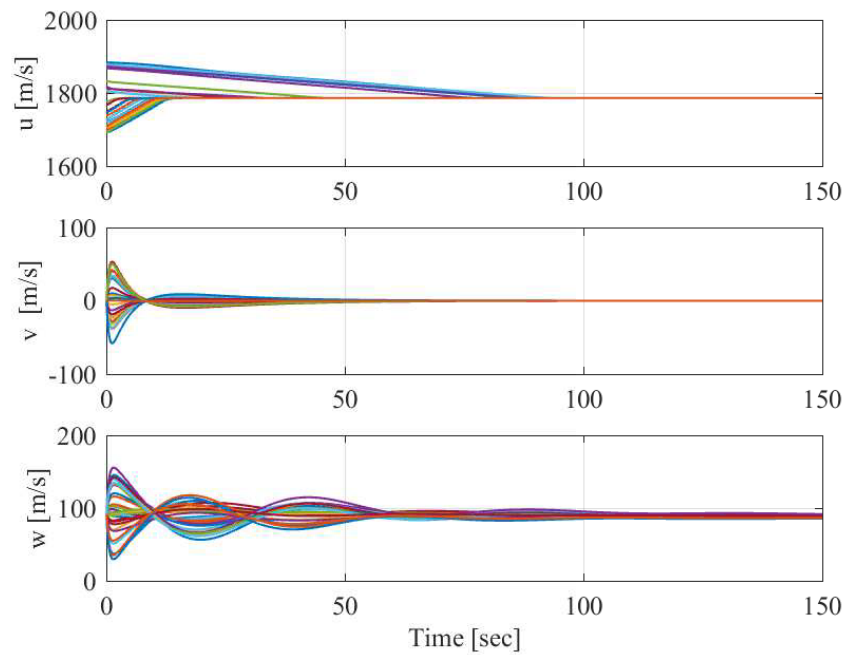


Figure 3.9 – Velocity Profiles  $u, v, w$  in  $x, y$ , and  $z$  Directions Respectively for Different Initial Conditions using Nominal Dynamic Inversion

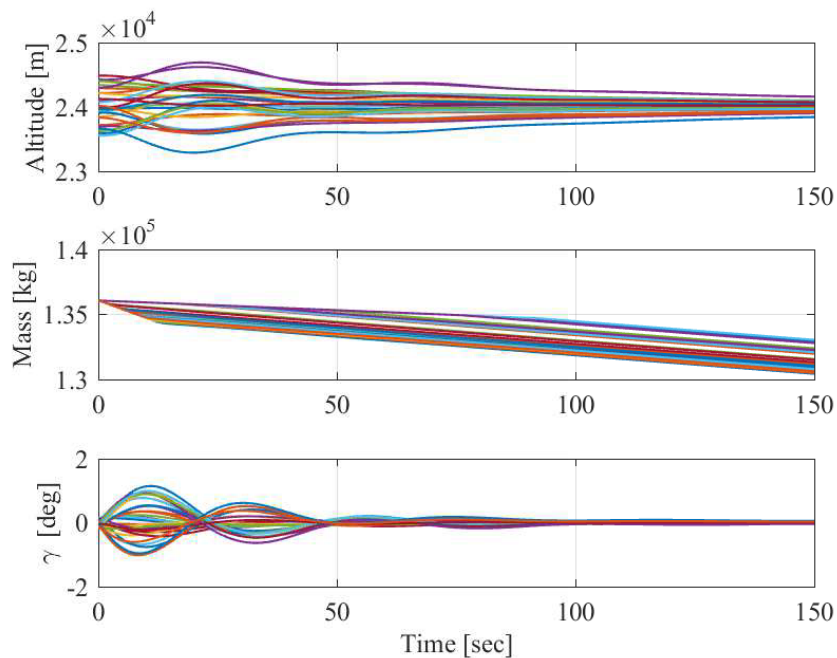


Figure 3.10 – Altitude ( $h$ ), Mass ( $M_v$ ) and Flight Path Angle ( $\gamma$ ) Profiles for Different Initial Conditions using Nominal Dynamic Inversion

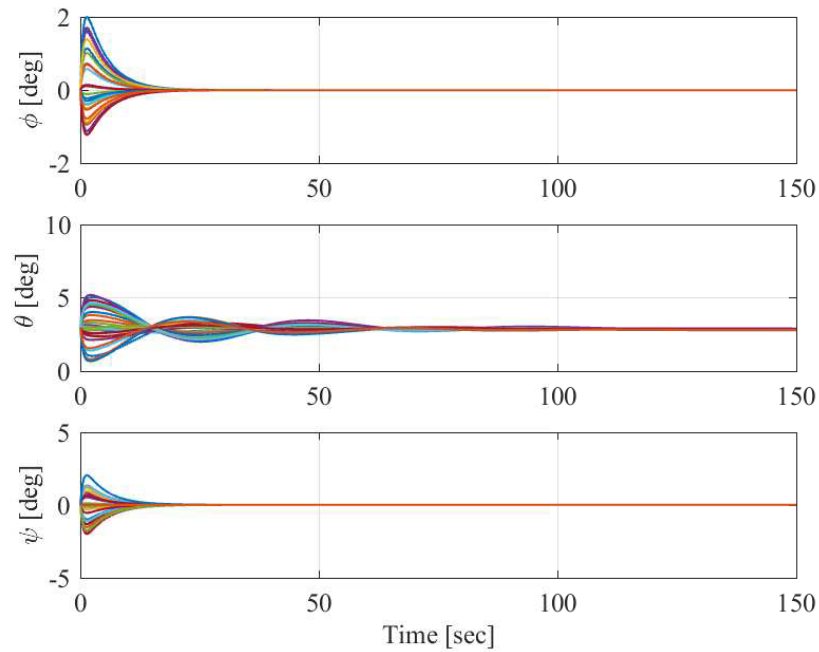


Figure 3.11 – Roll Angle ( $\phi$ ), Pitch Angle ( $\theta$ ), and Yaw Angle ( $\psi$ ) Profiles for Different Initial Conditions using Nominal Dynamic Inversion

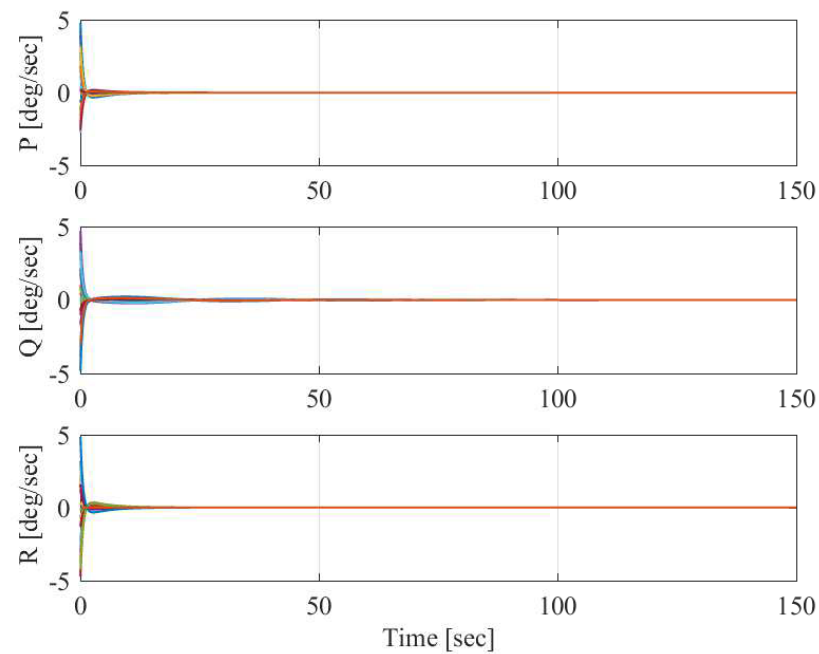


Figure 3.12 – Roll Rate ( $P$ ), Pitch Rate ( $Q$ ), and Yaw Rate ( $R$ ) Profiles for Different Initial Conditions using Nominal Dynamic Inversion

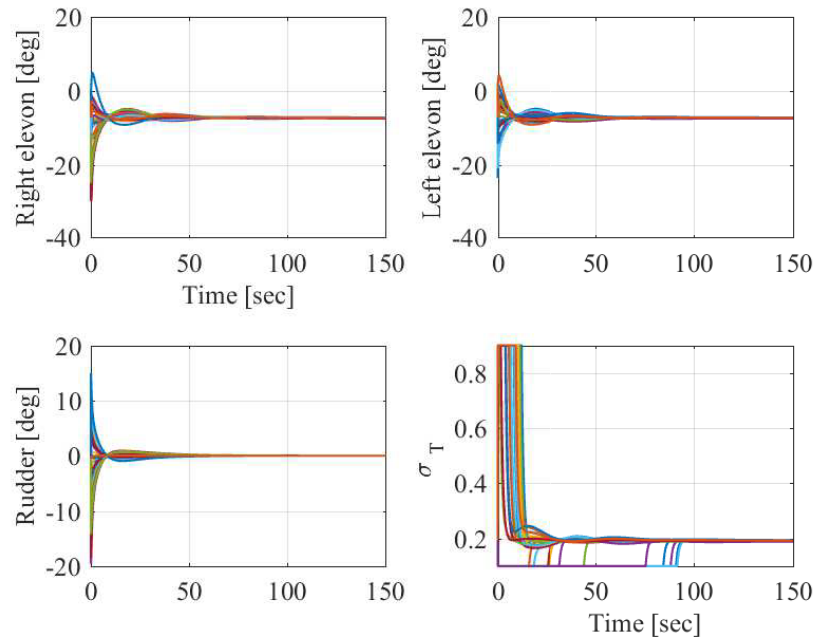


Figure 3.13 – Control Profiles for Different Initial Conditions using Nominal Dynamic Inversion

The angular angle and rate profiles are shown in Fig. 3.11 and Fig. 3.12 respectively for various initial conditions. All the state trajectories are converged to desired trajectories. Hence, the performance of designed nominal controller remains good for perturbed initial conditions and the AHV is stabilized for each initial condition. Finally, the control profiles are shown in Fig. 3.13, where all the control trajectories are smooth and within the saturation bound.

## 4 Neuro-adaptive Dynamic Inversion with Jacobian Learning

In this section, the formulation of adaptive controller using neuro-adaptive dynamic inversion technique is presented with necessary mathematical details. In neuro-adaptive DI technique, first, the nominal system model is assumed and the desired controller is obtained by using DI technique. Further, the actual model is approximated into an approximated system model and then using DI technique, the adaptive controller is designed by enforcing the error between the approximated and desired model to zero. The approximation of the actual system model and formulation of adaptive controller is explained in further sections.

### 4.1 Neuro-adaptive Dynamic Inversion Control Formulation

Consider a nonlinear nominal plant with completely known dynamics as

$$\dot{X}_d = f(X_d, U_d) \quad X_d \in \mathbb{R}^n, \quad U_d \in \mathbb{R}^m \quad (m \leq n) \quad (4.1)$$

here,  $U_d$  is the nominal control obtained from nominal dynamic inversion technique (chapter 3). However, in presence of external disturbance or parameter uncertainty, the nominal controller may not perform satisfactorily, hence, the adaptive controller is needed to maintain the performance of the vehicle.

The adaptive controller is formulated for the actual system model having model uncer-

tainties and disturbances. Hence, consider the nonlinear dynamics of the system as

$$\dot{X} = f(X, U) + d(X) \quad X \in \mathbb{R}^n, \quad U \in \mathbb{R}^m \quad (m \leq n) \quad (4.2)$$

where  $d(X)$  is the external disturbance or parameter uncertainties present in the system. In the neuro-adaptive technique, first the actual model is approximated by learning the disturbances presented in the actual model. Further, the Lyapunov method is used to obtain the disturbance learning rule. The approximated model of the actual system is considered as

$$\dot{X}_a = f(X, U) + \hat{d}(X) + k_{ap}(X - X_a) \quad X_a \in \mathbb{R}^n \quad (4.3)$$

here,  $\hat{d}(X)$  is the approximation of the disturbance  $d(X)$ , present in the actual system.  $k_{ap}$  is the positive definite matrix. Further, the error between the desired system and approximated system is enforced to zero by using linear error dynamics, as

$$\dot{X}_a - \dot{X}_d + k_{ad}(X_a - X_d) = 0 \quad (4.4)$$

here,  $k_{ad}$  is the positive definite matrix. Further, equation 4.4 is rearranged in a general form as

$$f(X, X_a, X_d, U, U_d, \hat{d}(X)) = 0 \quad (4.5)$$

The expression, obtained in equation 4.5, is the general expression to obtain the control. In the expression, the adaptive control  $U$  is obtained by using Newton-Raphson method, provided  $\hat{d}(X)$  is known. Further,  $\hat{d}(X)$  is obtained by weight update rule explained in section 4.2.

## 4.2 Constrained Weight Update Rule with Jacobian Learning

In this section the learning rule for  $\hat{d}(X)$  is derived, where,  $\hat{d}(X)$  is the approximation of the disturbance  $d(X)$ . Further, the error between the actual and approximated system is expressed



as

$$E = X - X_a \quad (4.6)$$

by differentiating equation 4.6, following is obtained

$$\dot{E} = \dot{X} - \dot{X}_a \quad (4.7)$$

further, substituting equations 4.2 and 4.3 into 4.7, the resulting expression is written as

$$\dot{E} = d(X) - \hat{d}(X) - k_{ap}(X - X_a) \quad (4.8)$$

further, for analysis purpose, the error is decomposed into individual channels as  $e_i = x_i - x_{i_a}$ , where,  $i = 1, 2, \dots, n$ . Hence, the  $i^{th}$  channel error dynamics can be written as

$$\dot{e}_i = d_i(X) - \hat{d}_i(X) - k_{i_{ap}}(e_i) \quad (4.9)$$

The disturbance is assumed to be linear in parameter form, hence

$$\begin{aligned} d_i(X) &= w_i^T \phi_i(X) + \epsilon_i \\ \hat{d}_i(X) &= \hat{w}_i^T \phi_i(X) \end{aligned}$$

here,  $\phi_i(X)$  is the basis function and  $w_i$  is the ideal unknown weights. Moreover,  $\hat{w}_i$  is the approximated weights and  $\epsilon_i$  is the approximation error.

Further, the error dynamics (4.9) can be written as

$$\dot{e}_i = \tilde{w}_i^T \phi_i(X) + \epsilon_i - k_{i_{ap}}(e_i) \quad (4.10)$$

where,  $\tilde{w}_i = w_i - \hat{w}_i$ , and further,  $\dot{\tilde{w}}_i = -\dot{\hat{w}}_i$ . Moreover, to obtain the learning rule, the

combination of BLF and QLF is selected for each channel as

$$V_i = \frac{1}{2} \log \frac{k_{b_i}^2}{k_{b_i}^2 - e_i^2} + \frac{\tilde{w}_i^T \tilde{w}_i}{2\gamma_i} + \left[ \frac{\partial d_i(X)}{\partial X} - \frac{\partial \hat{d}_i(X)}{\partial X} \right]^T \frac{\Theta_i}{2} \left[ \frac{\partial d_i(X)}{\partial X} - \frac{\partial \hat{d}_i(X)}{\partial X} \right] \quad (4.11)$$

here,  $k_{b_i}$ ,  $\gamma_i$ , and  $\Theta_i$  are the positive definite quantities and  $\gamma_i$  is a positive constant known as learning rate. Moreover,  $\frac{\partial d_i(X)}{\partial X}$  and  $\frac{\partial \hat{d}_i(X)}{\partial X}$  are the jacobian matrices of the disturbance function and its approximation, which are used to minimize the transients. Further, the BLF is used to constrained the error  $e_i$  within a constant positive bound  $|k_{b_i}|$ .

further, taking the derivative of the Lyapunov function (4.11) and rearranging the components, following is obtained

$$\begin{aligned} \dot{V}_i = & \tilde{w}_i^T \left[ \frac{e_i \phi_i(X)}{k_{b_i}^2 - e_i^2} - \frac{\hat{w}_i}{\gamma_i} - \left[ \frac{\partial \phi_i}{\partial X} \right] \Theta_i \left[ \frac{\partial \phi_i}{\partial X} \right]^T \hat{w}_i \right] \\ & + \frac{e_i \epsilon_i}{k_{b_i}^2 - e_i^2} - \frac{k_{i_{ap}} e_i^2}{k_{b_i}^2 - e_i^2} + \tilde{w}_i^T \left[ \frac{\partial \phi_i}{\partial X} \right] \Theta_i \frac{d}{dt} \left[ \frac{\partial \phi_i}{\partial X} \right]^T \tilde{w}_i \end{aligned} \quad (4.12)$$

here,  $\frac{\partial \phi_i}{\partial X}$  is the jacobian matrices of the basis function. Further, by equating  $\tilde{w}_i^T = 0$ , the weight update rule is obtained as

$$\dot{\hat{w}}_i = \left[ \frac{I_p}{\gamma_i} + \left[ \frac{\partial \phi_i}{\partial X} \right] \Theta_i \left[ \frac{\partial \phi_i}{\partial X} \right]^T \right]^{-1} \frac{e_i \phi_i(X)}{k_{b_i}^2 - e_i^2} \quad (4.13)$$

here,  $I_p$  is the identity matrix of dimension  $p$ . Further, the  $\hat{d}_i(X)$  is obtained by the expression  $\hat{d}_i(X) = \hat{w}_i^T \phi_i(X)$ . Moreover, the further analysis of  $\dot{V}_i$  equation (4.12) can be found in the literature published by [Ambati and Padhi \[2016\]](#), in which, the boundedness of the error is shown mathematically.

### 4.3 Simulation Results

In this section, the simulation results are presented with the application of adaptive controller on the actual system obtained by neuro-adaptive DI technique. The model uncertainties are assumed in the aerodynamic coefficients and in the inertia values. The disturbance is added

in  $\dot{P}$ ,  $\dot{Q}$ , and  $\dot{R}$  state equations. The initial conditions are given as,  $V_t = 1789 \text{ m/s}$ ,  $\alpha = 2.94 \text{ deg}$ ,  $\beta = 0 \text{ deg}$ ,  $P = 0 \text{ deg/sec}$ ,  $Q = 0 \text{ deg/sec}$ ,  $R = 0 \text{ deg/sec}$ ,  $\phi = 0 \text{ deg}$ ,  $\theta = 2.94 \text{ deg}$ ,  $\psi = 0 \text{ deg}$ ,  $x = 0 \text{ m}$ ,  $y = 0 \text{ m}$ ,  $h = 24000 \text{ m}$  and initial mass  $M_v = 136077.6 \text{ kg}$ . The inner loop gains  $k_P$ ,  $k_Q$ , and  $k_R$  are selected as 2.0 and the intermediate loop gains  $k_\phi$ ,  $k_\theta$ , and  $k_\psi$  are selected as 0.1. The outer loop control gain  $k_h$  is selected as 0.01 and further, the velocity loop controller gain is chosen as 0.1.

The disturbance learning rate  $\gamma_i$  is selected as 40 and the constraint on the error (equation 4.6) is selected as,  $0.7 \text{ deg/sec}$ . The positive definite matrix  $k_{ad}$  used in equation 4.4 is selected as  $\text{diag}(5, 7, 5)$  and  $k_{ap}$  used in equation 4.3 is selected as  $\text{diag}(15, 18, 15)$ . Here, the gain values of  $k_{ap}$  is more than  $k_{ad}$  so that  $x \rightarrow x_a$  (very quickly) before  $x_a \rightarrow x_d$ . Further, the simulation is carried out for random disturbance within 30% of model uncertainty. Furthermore, the basis functions  $\phi(x)$  is selected as  $[1, P, P^2, Q, Q^2, (PQ)^2, R, R^2, (PR)^2, (QR)^2, (PQR)^2]$  and the Jacobian matrix of the basis function  $\left[\frac{\partial \phi}{\partial x}\right]$  is calculated as

$$\left[\frac{\partial \phi}{\partial x}\right] = \begin{bmatrix} 0 & 1 & 2P & 0 & 0 & 2PQ^2 & 0 & 0 & 2PR^2 & 0 & 2PQ^2R^2 \\ 0 & 0 & 0 & 1 & 2Q & 2P^2Q & 0 & 0 & 0 & 2QR^2 & 2P^2QR^2 \\ 0 & 0 & 0 & 0 & 0 & 0 & 1 & 2R & 2P^2R & 2Q^2R & 2P^2Q^2R \end{bmatrix}^T \quad (4.14)$$

Further, the velocity, angle of attack and sideslip angle profiles are shown in Fig. 4.1 respectively. In the plots, the profiles obtained using nominal control for actual system are become unbounded, hence, the nominal controller is not effective in presence of uncertainties. Further, the desired trajectories are effectively tracked by the obtained profiles with the application of adaptive controller. Moreover, the angle of attack is within the bound and the constant velocity is maintained by the velocity controller to prevent the inlet unstart.

Similarly, the constant height is maintained by the adaptive controller as shown in the Fig. 4.2. The mass profile is smooth and continuous and the flight path angle profile is stabilized at zero. Further, the roll, pitch, and yaw angle profiles are presented in Fig. 4.3 respectively. The states are bounded and tracking the desired states. Moreover, the pitch angle is non-zero to achieve the required lift in the vehicle.

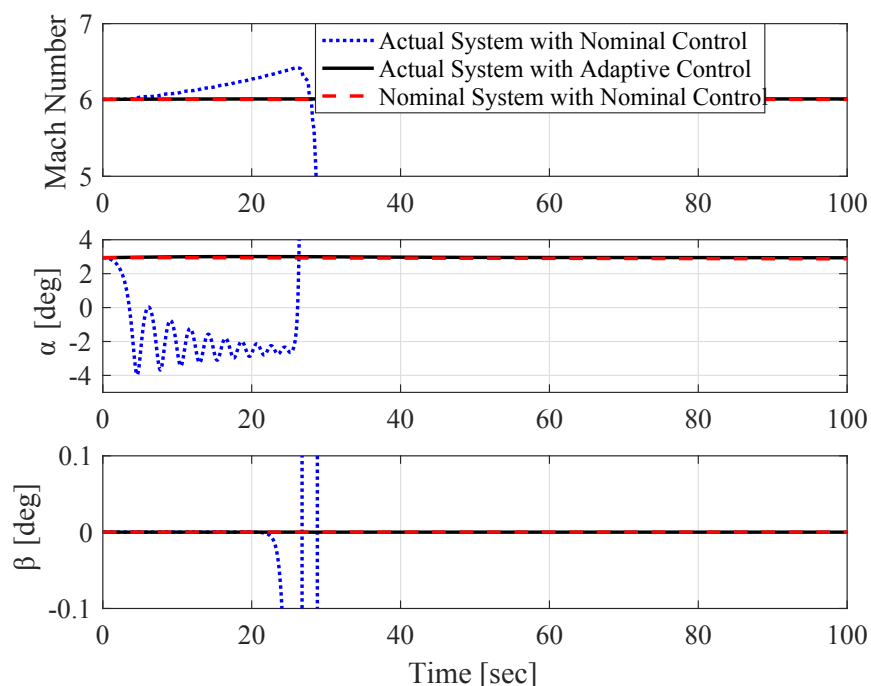


Figure 4.1 – Mach Number ( $M$ ), Angle of Attack ( $\alpha$ ) and Sideslip Angle ( $\beta$ ) Profiles of AHV using Neuro-adaptive Dynamic Inversion

The angular rate profiles are shown in Fig. 4.4 respectively. After some transients, the angular rate profiles are tracking the desired states perfectly, which means AHV is stable. Hence, the formulated neuro-adaptive DI controller is effective to control the uncertain AHV. Further, the control profiles are shown in Fig. 4.5. The control surface deflections are continuous (zoomed in box) and within the saturation limits hence, the solution provided by the controller is physically realizable. Further, the neuro-adaptive DI control profiles are different from the nominal DI control profiles because of the uncertainty presents in the system.

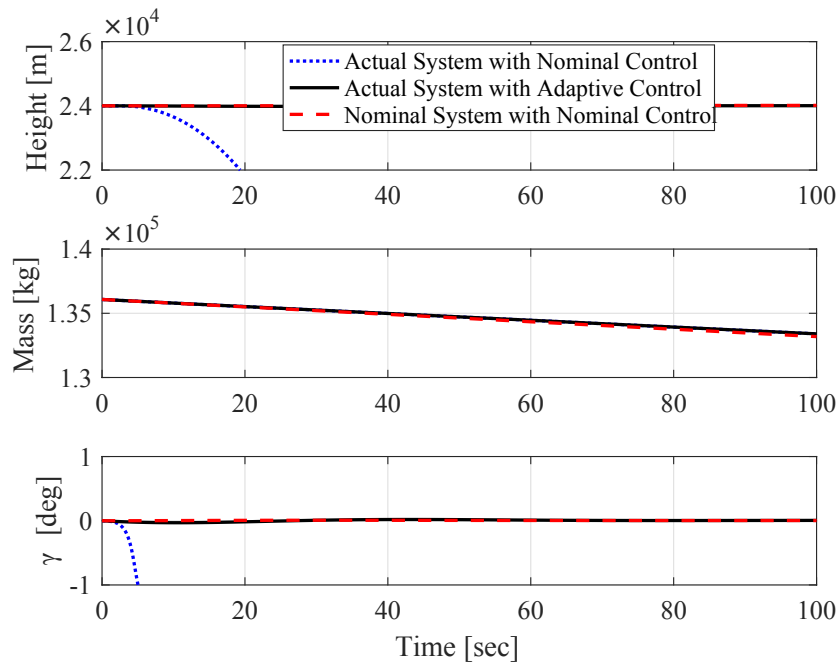


Figure 4.2 – Altitude ( $h$ ), Mass ( $M_v$ ) and Flight Path Angle ( $\gamma$ ) Profiles of AHV using Neuro-adaptive Dynamic Inversion

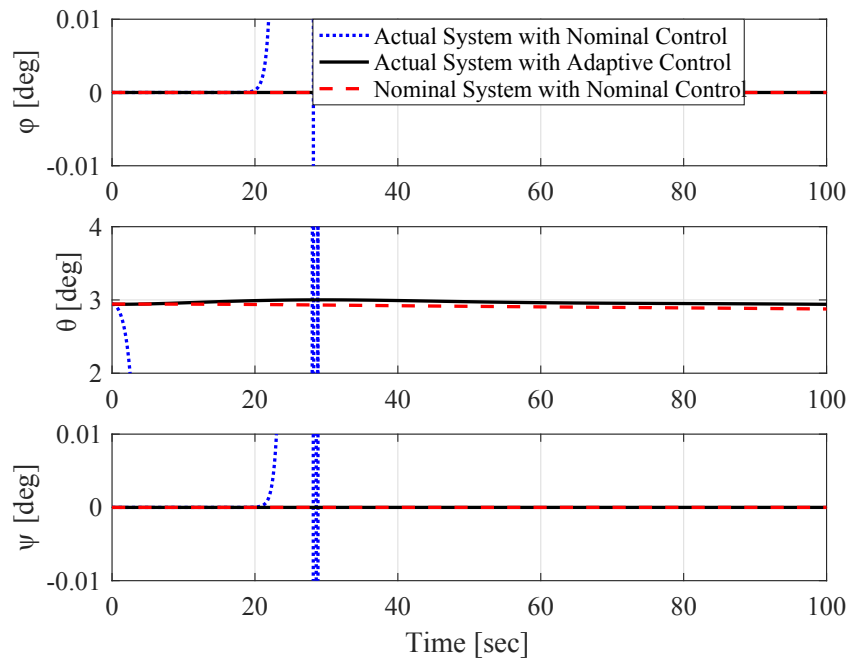


Figure 4.3 – Roll Angle ( $\phi$ ), Pitch Angle ( $\theta$ ), and Yaw Angle ( $\psi$ ) Profiles of AHV using Neuro-adaptive Dynamic Inversion

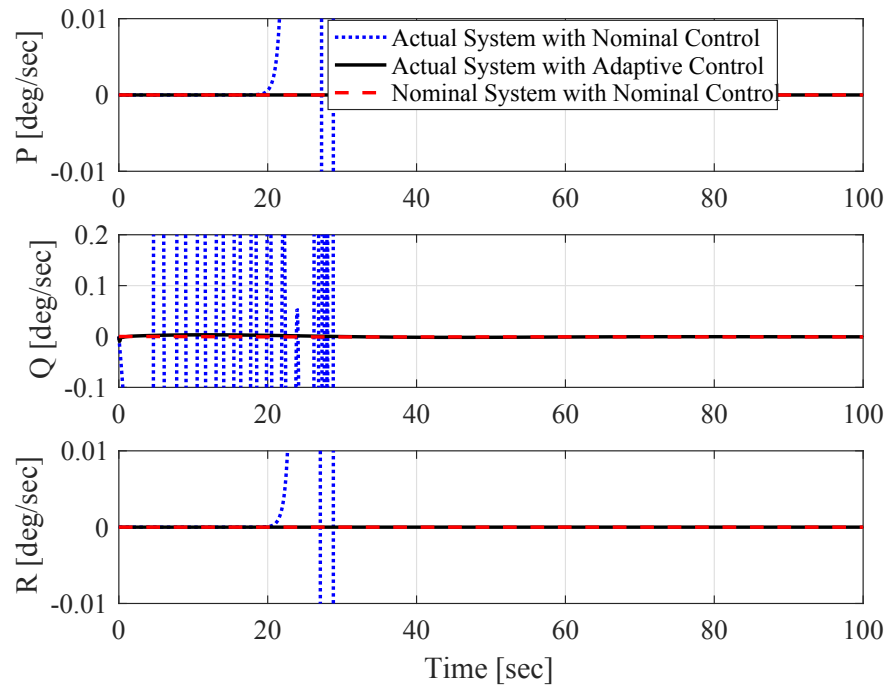


Figure 4.4 – Roll Rate ( $P$ ), Pitch Rate ( $Q$ ), and Yaw Rate ( $R$ ) Profiles of AHV using Neuro-adaptive Dynamic Inversion

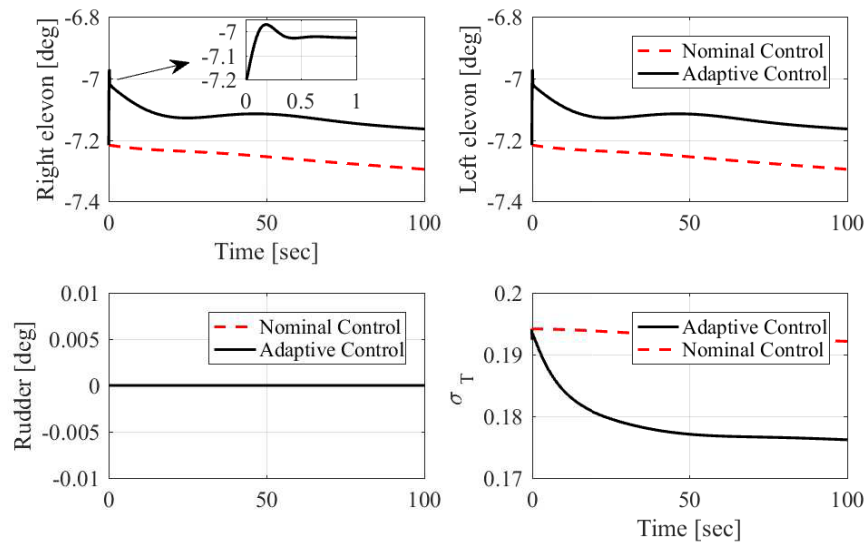


Figure 4.5 – Control Profiles obtained using Neuro-adaptive Dynamic Inversion

Further, the simulation results are presented for random disturbances bounded between  $[-30\%, 30\%]$ . The velocity and angle of attack profiles are shown in Fig. 4.6 for the AHV. The inlet unstart condition is successfully prevented by the proposed controller because the angle of attack is perfectly bounded between  $[-5^\circ, 5^\circ]$  and velocity level is maintained accordingly. The altitude and mass profiles for AHV are shown in Fig. 4.7. The smooth and continuous profiles are obtained in random disturbances shows the applicability of the adaptive controller.

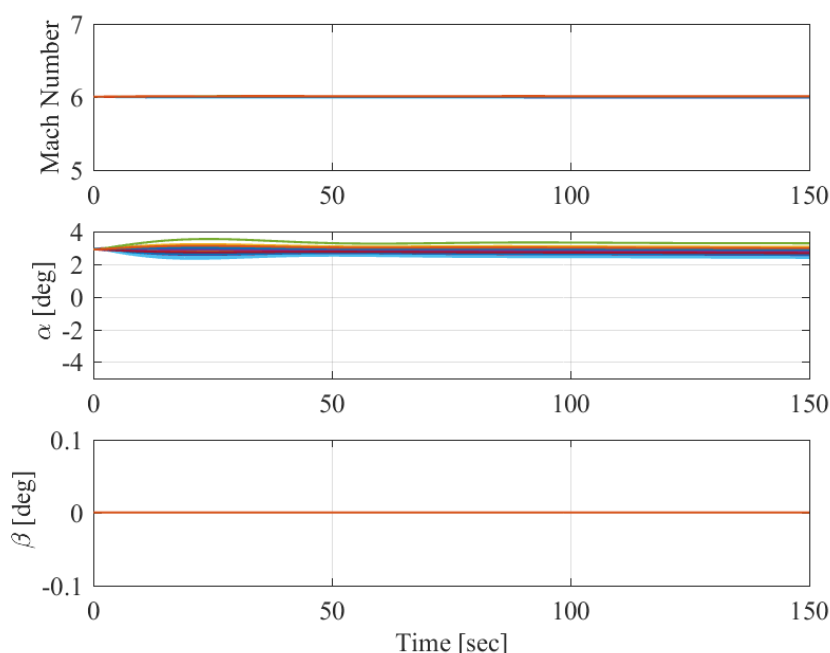


Figure 4.6 – Mach Number ( $M$ ), Angle of Attack ( $\alpha$ ) and Sideslip Angle ( $\beta$ ) Profiles for Random Disturbances using Neuro-adaptive Dynamic Inversion

The angular angles rates profiles are shown in Fig. 4.8 and Fig. 4.9 respectively for the AHV. All the state trajectories converged to desired trajectories within finite time with very minimal transients. Hence, the designed adaptive controller stabilized the AHV in presence of model uncertainties. Finally, the control profiles are shown in Fig. 4.10, where, all the trajectories are smooth and achievable by control surfaces. The magnitude of the required control is depend on the level of model uncertainty.

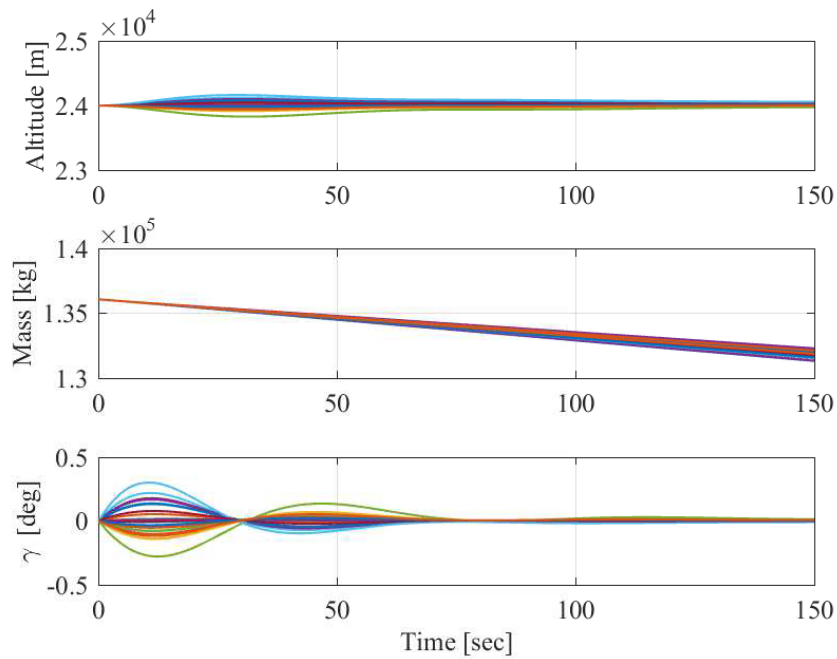


Figure 4.7 – Altitude ( $h$ ), Mass ( $M_v$ ) and Flight Path Angle ( $\gamma$ ) Profiles for Random Disturbances using Neuro-adaptive Dynamic Inversion

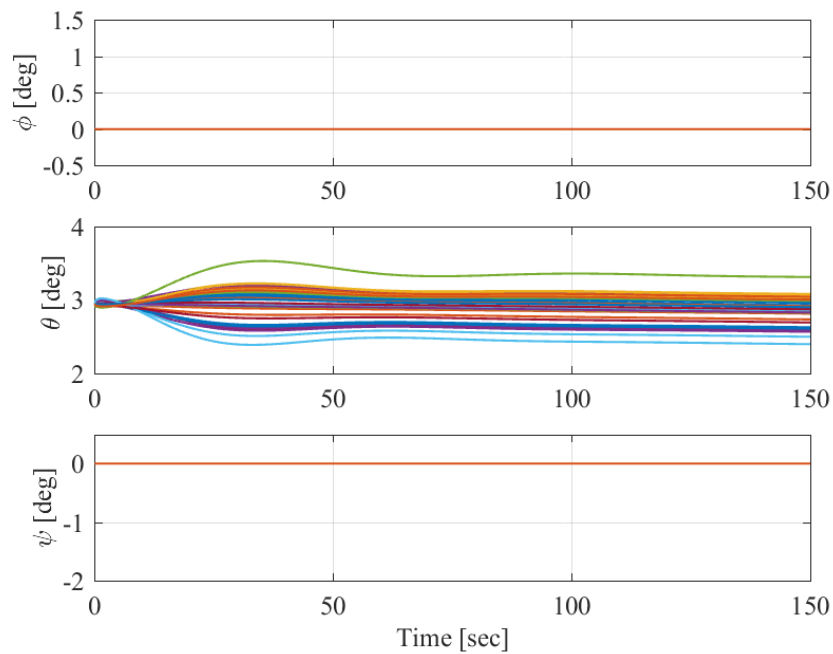


Figure 4.8 – Roll Angle ( $\phi$ ), Pitch Angle ( $\theta$ ), and Yaw Angle ( $\psi$ ) Profiles for Random Disturbances using Neuro-adaptive Dynamic Inversion



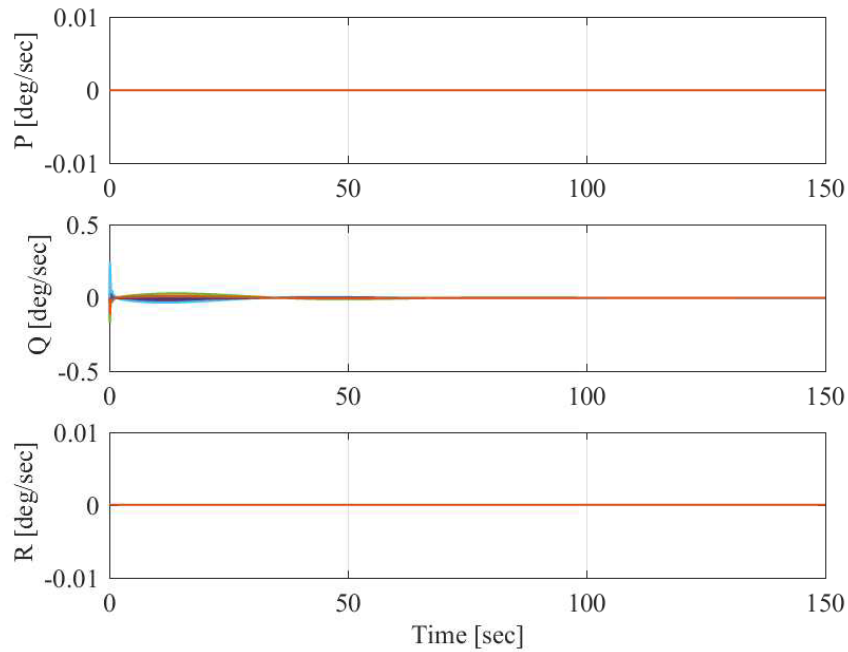


Figure 4.9 – Roll Rate ( $P$ ), Pitch Rate ( $Q$ ), and Yaw Rate ( $R$ ) Profiles for Random Disturbances using Neuro-adaptive Dynamic Inversion

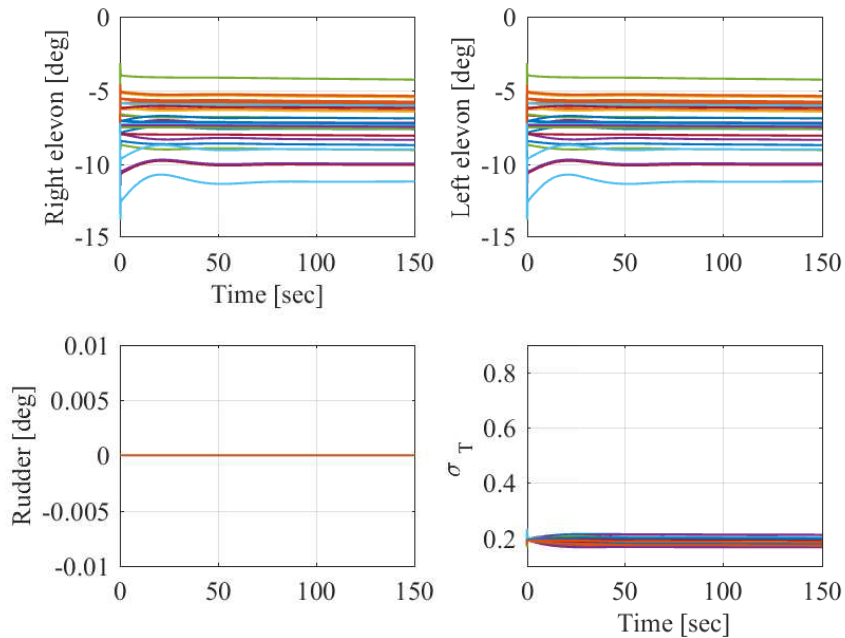


Figure 4.10 – Control Profiles obtained for Random Disturbances using Neuro-adaptive Dynamic Inversion

# 5 Neuro-adaptive Generalized Dynamic Inversion with Jacobian Learning

## 5.1 Neuro-adaptive State-constrained Generalized Dynamic Inversion Formulation

In this section, first the state-constrained generalized dynamic inversion (SC-GDI) formulation is presented for controlling the nonlinear system given in equation 4.2. In the formulation, barrier Lyapunov function (BLF) is selected as the lyapunov candidate for incorporating the state constraint on the states. Further, it has been shown that the dynamic inversion technique is a subset of SC-GDI and by selecting a tuning variable, the SC-GDI is converted into DI. Further, it has been shown that the obtained controller is robust enough to maintain the constraint on states in presence of disturbances, however, to achieve perfect tracking, SC-GDI is augmented with disturbance learning mechanism. Since the disturbance learning rule is already explained in section 5.3, hence, in this chapter, only the formulation of SC-GDI technique and the derivation of neuro-adaptive SC-GDI control is presented.

### 5.1.1 Formulation of State-Constrained Generalized Dynamic Inversion

State-constrained generalized dynamic inversion formulation is shown in this section for an ideal system (no uncertainty). In this section, therefore, general nonlinear system, given in equation 4.2, is considered by assuming  $d(X) = 0$ . Further, it has been assumed that the dimension of control ( $U \in \mathbb{R}^m$ ), states ( $X \in \mathbb{R}^n$ ) and output ( $Y \in \mathbb{R}^m$ ) are same i.e.,  $p = m = n$ .

This assumption is relevant in AHV control study because the disturbance is assumed in  $\dot{P}$ ,  $\dot{Q}$ , and  $\dot{R}$  state equations (2.3), hence, the output  $(P, Q, R)$ , states  $(P, Q, R)$  and controls  $(\delta_e, \delta_a, \delta_r)$  are equal. Moreover, without loss of generality, the problem is assumed as a regulation problem, which is also relevant too in AHV control because, the desired  $P_d^*$ ,  $Q_d^*$  and  $R_d^*$  are always zero.

Further, the error equation is defined as

$$E = Y \quad (5.1)$$

for the purpose of analysis, the error  $(E \in \mathbb{R}^n)$  equation (5.1) is decomposed into individual channels. Hence, the the error equation is given as

$$e_j = y_j, \quad j = 1, 2, \dots, m \quad (5.2)$$

$$e_i = y_i, \quad i = m + 1, m + 2, \dots, n \quad (5.3)$$

The combination of barrier Lyapunov function (BLF) and quadratic Lyapunov function (QLF) is selected as the Lyapunov function candidate. The BLF is chosen for the states having constraint  $(x_j)$  and QLF is selected to maintain the boundedness of the remaining states  $x_i$ . Hence, the Lyapunov function is written as

$$V = \frac{1}{2} \sum_{j=1}^m \log \frac{k_{s_j}^2}{k_{s_j}^2 - e_j^2} + \frac{1}{2} \sum_{i=m+1}^n e_i^2 \quad (5.4)$$

here,  $k_{s_j}$  is the positive constant, selected as the constraint on  $e_j$  i.e.,  $e_j < |k_{s_j}| \forall t \geq 0$ . Further, the derivative of the Lyapunov function (5.4) can be obtained as

$$\dot{V} = \sum_{j=1}^m \frac{\dot{e}_j e_j}{k_{s_j}^2 - e_j^2} + \sum_{i=m+1}^n \dot{e}_i e_i \quad (5.5)$$

further, for compact analysis, equation 5.5 is written into vector format as

$$\dot{V} = (B_L E)^T \dot{E} \quad (5.6)$$

where  $E = [e_1, e_2, \dots, e_n]^T$  and  $[B_L] \in \mathbb{R}^{n \times n}$  is a symmetric diagonal matrix, given as

$$[B_L] = \text{diag} \left( \frac{1}{k_{s_1}^2 - e_1^2}, \frac{1}{k_{s_2}^2 - e_2^2}, \dots, \frac{1}{k_{s_m}^2 - e_m^2}, 1, \dots, 1 \right) \quad (5.7)$$

By using Lyapunov stability theory, for a stable close loop system ( $\dot{V} < 0$ ). The stability of the system is enforced by equating  $\dot{V}$  with a negative definite function, defined as

$$\dot{V} = -E^T K_{blf} E \quad (5.8)$$

where,  $[K_{blf}] \in \mathbb{R}^{n \times n}$  is a positive definite symmetric diagonal matrix expressed as

$$[K_{blf}] = \text{diag} \left( \frac{k_1}{(k_{s_1}^2 - e_1^2)^\lambda}, \dots, \frac{k_m}{(k_{s_m}^2 - e_m^2)^\lambda}, k_{m+1}, \dots, k_n \right)$$

here,  $[K_{blf}] > 0$ ,  $\forall t > 0$  because  $k_{s_i} > e_i$ ,  $\forall t \geq 0$  (Tee et al. [2009]) and  $k_1, k_2, \dots, k_n$  are selected as positive constants. Further,  $\lambda \in \mathbb{R}$  and  $\lambda$  can be different for different terms in  $[K_{blf}]$ , however, for simplicity unique value of  $\lambda$  has been selected in this report. Further, by equating the equation 5.6 with 5.8, one can obtain

$$(B_L E)^T \dot{E} = -E^T K_{blf} E \quad (5.9)$$

Since  $B_L^T = B_L$  hence, equation 5.9 can be rewritten as

$$E^T B_L \dot{E} = -E^T K_{blf} E \quad (5.10)$$

Finally, the error dynamics can be obtained as

$$\dot{E} + B_L^{-1} K_{blf} E = 0 \quad (5.11)$$

where  $[B_L^{-1} K_{blf}] \in R^{n \times n}$  given as,

$$[B_L^{-1} K_{blf}] = \text{diag} \left( \frac{k_1}{(k_{s_1}^2 - e_1^2)^{\lambda-1}}, \dots, \frac{k_m}{(k_{s_m}^2 - e_m^2)^{\lambda-1}}, \dots, k_n \right)$$

Here, equation 5.11 is known as the nonlinear error dynamic equation, used for control calculation. Further for control calculation, equation 5.11 is rewritten by using equation 5.1 and expressed as,

$$\dot{X} + B_L^{-1} K_{blf} X = 0 \quad (5.12)$$

Hence, the general expression for obtaining the control is given as

$$f(X, U) + B_L^{-1} K_{blf} X = 0$$

Hence, by using the Newton-Raphson method, the control  $U$  is obtained. Further, if the system dynamics is in control affine form i.e.,  $\dot{X} = f(X) + g(X)U$ , where,  $f(X)$  and  $g(X)$  are nonlinear, smooth function of  $X$ , then the state-constrained control solution  $U$  is obtained as

$$U = [g(X)]^{-1} (-B_L^{-1} K_{blf} X - f(X)) \quad (5.13)$$

**Note.** By careful observation, it can be seen that by selecting  $\lambda = 1$  in  $B_L^{-1} K_{blf}$  expression, the error dynamics (5.11) and the control (5.13) transformed into the error dynamics and control obtained from regular dynamic inversion formulation (Padhi et al. [2007]). The regular dynamic inversion control technique, therefore, is a subset of proposed technique. Furthermore,  $B_L^{-1} K_{blf}$  matrix is always a positive definite matrix, hence, the nonlinear error dynamics (5.11) is always be stable. Hence, the proposed technique is named as state-constrained generalized

nonlinear dynamic inversion (SC-GDI) control technique.

### 5.1.2 Neuro-adaptive SC-GDI Control Formulation

In this section, The formulation of adaptive control using neuro-adaptive SC-GDI technique is presented for an uncertain system. The desired nominal plant and approximated model plant dynamics is shown in equations 4.1 and 4.3 respectively. Hence, by using equation 5.11, the nonlinear error dynamics can be written as

$$\dot{X}_a - \dot{X}_d + B_L^{-1} K_{blf} (X_a - X_d) = 0 \quad (5.14)$$

here,  $B_L^{-1} K_{blf}$  is the positive definite matrix. Further, equation 5.14 is rearranged in a general form as

$$f(X, X_a, X_d, U, U_d, \hat{d}(X)) = 0 \quad (5.15)$$

here, the equation 5.15 is the general expression to obtain the neuro-adaptive SC-GDI control. Further,  $U_d$  is the desired control formulated in subsection 5.1.1. Moreover, In the expression (5.15), the adaptive control  $U$  is obtained by using Newton-Raphson method provided  $\hat{d}(X)$  is known. Further,  $\hat{d}(X)$  is obtained by weight update rule explained in section 4.2.

## 5.2 Simulation Results

In this section, the simulation results are presented with the application of neuro-adaptive SC-GDI control on the actual system. The model uncertainty is assumed in the aerodynamic forces and moments coefficients and in the inertia values. The disturbance is added in  $\dot{P}$ ,  $\dot{Q}$ , and  $\dot{R}$  state equations. The initial condition values assumed in the simulations are given as,  $V_t = 1789 \text{ m/s}$ ,  $\alpha = 2.94 \text{ deg}$ ,  $\beta = 0 \text{ deg}$ ,  $P = 0 \text{ deg/sec}$ ,  $Q = 0 \text{ deg/sec}$ ,  $R = 0 \text{ deg/sec}$ ,  $\phi = 0 \text{ deg}$ ,  $\theta = 2.94 \text{ deg}$ ,  $\psi = 0 \text{ deg}$ ,  $x = 0 \text{ m}$ ,  $y = 0 \text{ m}$ ,  $h = 24000 \text{ m}$  and initial mass  $M_v = 136077.6 \text{ kg}$ . The inner loop gains  $k_P$ ,  $k_Q$ , and  $k_R$  are selected as 2.0. Moreover,  $\lambda$  and  $k_s$  values

(5.11) for  $\dot{P}$ ,  $\dot{Q}$ ,  $\dot{R}$  states are selected as,  $[0.001^\circ, 0.001^\circ, 0.001^\circ]$  and 0.1, 0.3, 0.1 respectively. Further, the intermediate loop gains  $k_\phi$ ,  $k_\theta$ , and  $k_\psi$  are selected as 0.1. The outer loop control gain  $k_h$  is selected as 0.01 and further, the velocity loop controller gain is chosen as, 0.1.

The positive definite matrix  $k_{ad}$  used in equation 4.4 is selected as  $diag(5, 7, 5)$  and  $k_{ap}$  used. The disturbance learning rate  $\gamma_i$  is selected as 40 and the constraint on the error (equation 4.6) is selected as  $0.7deg/sec$ . Further, the simulation is carried out for a random disturbance bounded within 30% of model uncertainty. Moreover, the basis functions  $\phi(x)$  is selected as  $[1, P, P^2, Q, Q^2, (PQ)^2, R, R^2, (PR)^2, (QR)^2, (PQR)^2]$  and the Jacobian matrix of the basis function  $\left[\frac{\partial\phi}{\partial x}\right]$  is already given in equation 4.14.

In the simulations, three type of plots are presented, the first plot is obtained by the application of nominal controller on nominal dynamics, further, the second plot is obtained by the application of nominal controller on actual system dynamics and finally, third plot is obtained by the application of adaptive controller on the actual system. It can be seen from the plots that nominal controller is not effective for the actual system and results into an unstable AHV. The velocity, angle of attack and sideslip angle profiles are shown in Fig. 5.1 respectively with the application of adaptive controller. The effectiveness of the adaptive controller is seen by the plots where the desired states of system are perfectly tracked by the actual states of system. Further, the angle of attack profile is bounded within the limits  $[-5^\circ, 5^\circ]$  and constant velocity is maintained by the velocity controller to prevent the inlet unstart.

Further, the altitude of the AHV is maintained close to the reference altitude by the application of SC-GDI adaptive controller, as shown in the height plot of Fig. 5.2. The mass profile is smooth and continuous which means that there is no sudden thrust requirement during the flight. Moreover, the flight path angle profile is stabilized at zero by the application of adaptive control. Further, the roll, pitch, and yaw angle profiles are presented in Fig. 5.3 respectively. All the angle profiles are bounded and the error between the desired states and the actual states become zero in finite time.

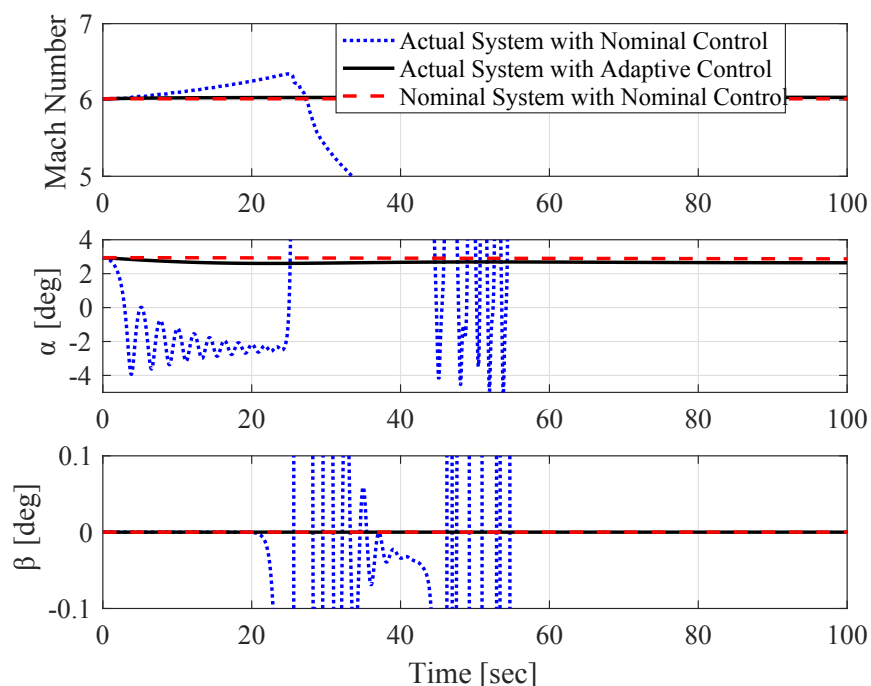


Figure 5.1 – Mach Number ( $M$ ), Angle of Attack ( $\alpha$ ) and Sideslip Angle ( $\beta$ ) Profiles of AHV using Neuro-adaptive Generalized Dynamic Inversion

Further, the roll, pitch and yaw rate profiles are shown in Fig. 5.4 respectively. All the angular rate profiles are converged quickly towards the desired states, which means that the AHV is stabilized by using the derived adaptive controller. Hence, the formulated neuro-adaptive SC-GDI controller is effective for controlling the uncertain AHV. Further, the adaptive control profiles are shown in Fig. 5.5. The control surface deflections are smooth and continuous (shown in zoomed in box) and within the saturation limits hence, the solution provided by the SC-GDI controller is physically achievable.



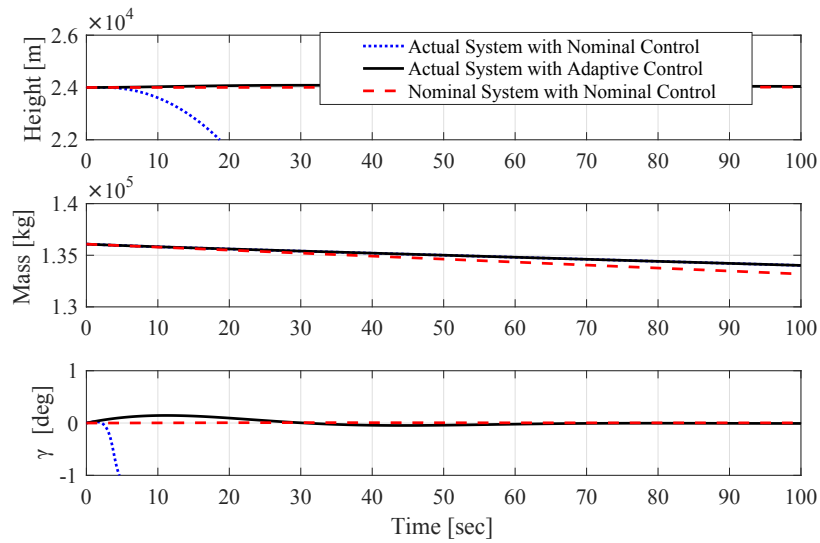


Figure 5.2 – Altitude ( $h$ ), Mass ( $M_v$ ) and Flight Path Angle ( $\gamma$ ) Profiles of AHV using Neuro-adaptive Generalized Dynamic Inversion

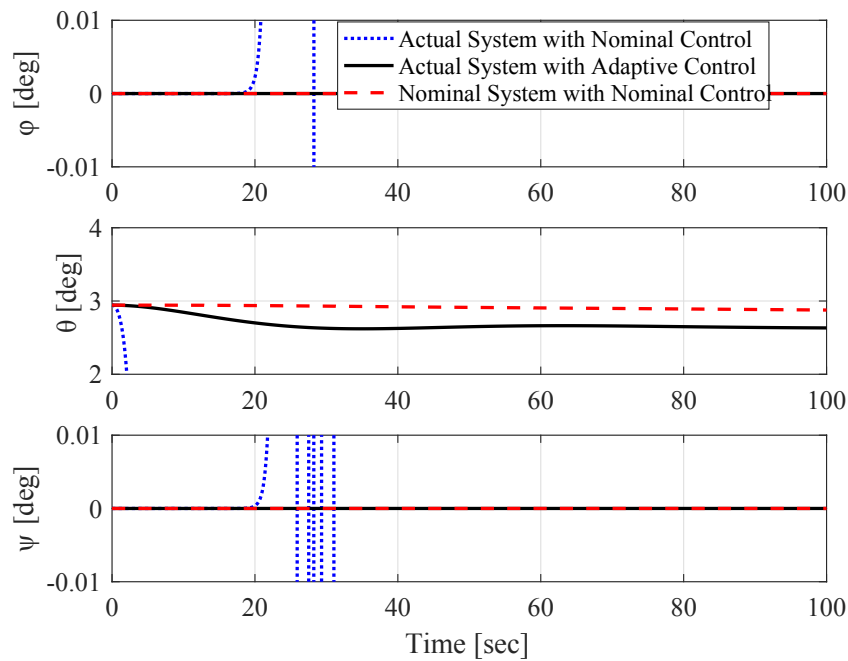


Figure 5.3 – Roll Angle ( $\phi$ ), Pitch Angle ( $\theta$ ), and Yaw Angle ( $\psi$ ) Profiles of AHV using Neuro-adaptive Generalized Dynamic Inversion

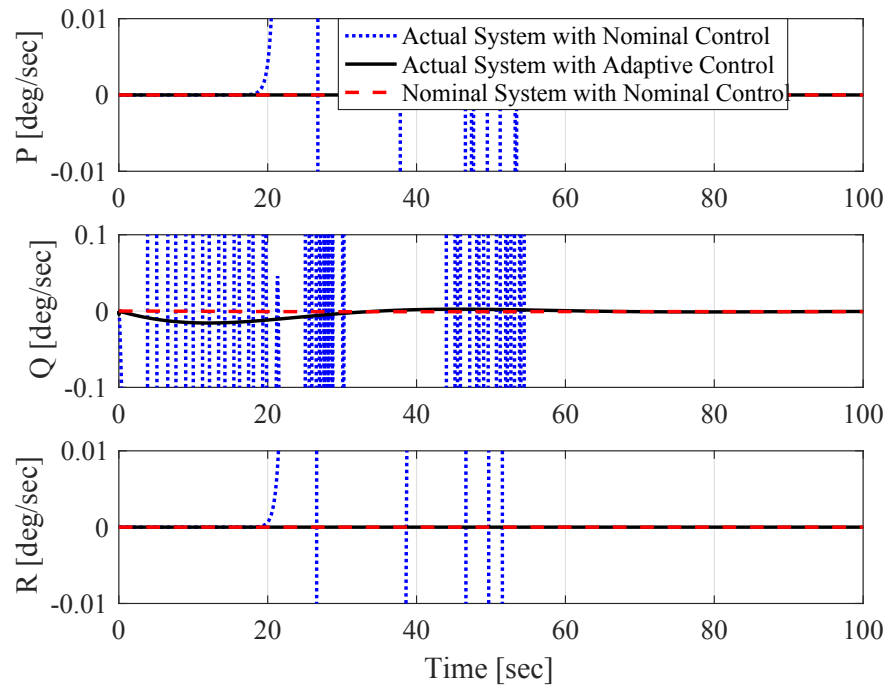


Figure 5.4 – Roll Rate ( $P$ ), Pitch Rate ( $Q$ ), and Yaw Rate ( $R$ ) Profiles of AHV using Neuro-adaptive Generalized Dynamic Inversion

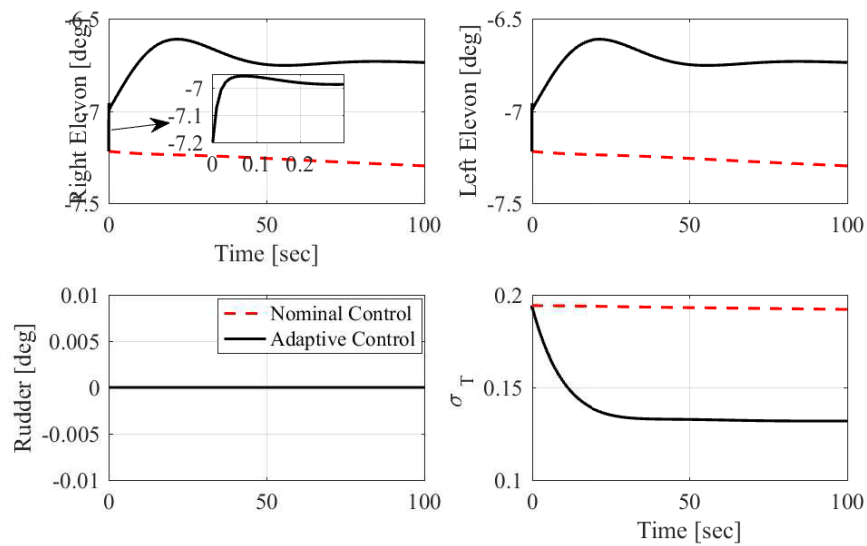


Figure 5.5 – Control Profiles obtained using Neuro-adaptive Generalized Dynamic Inversion

Further, the simulation results are presented for random bounded disturbances between  $[-30\%, 30\%]$ . The velocity, angle of attack and sideslip angle profiles are shown in Fig. 5.6 for uncertain AHV. The inlet unstart condition is successfully prevented by the proposed controller because the angle of attack is perfectly bounded between  $[-5^\circ, 5^\circ]$  and velocity level is maintained accordingly. The altitude and mass profiles for AHV are shown in Fig. 5.7 respectively. The smooth and continuous profiles are obtained in presence of random disturbances shows the applicability of the adaptive controller.

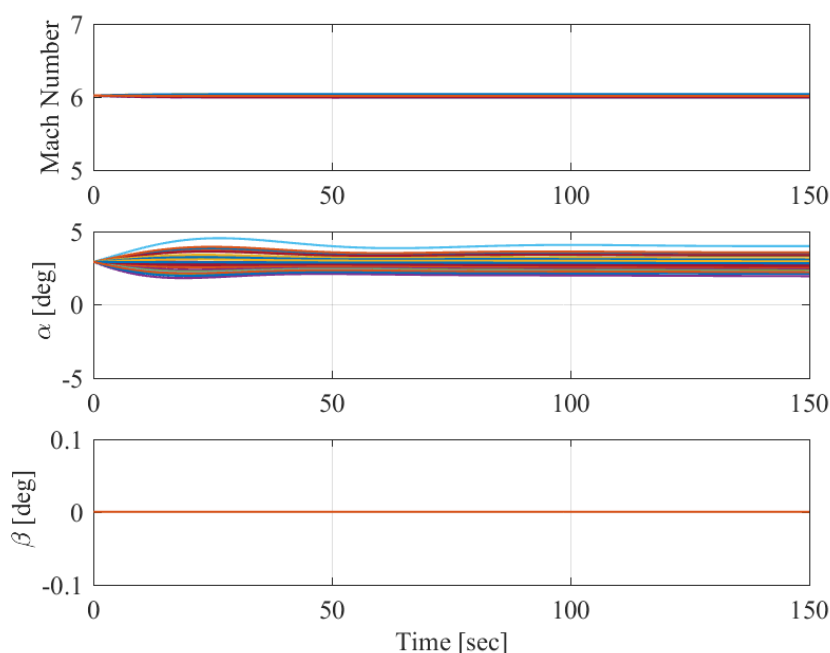


Figure 5.6 – Mach Number ( $M$ ), Angle of Attack ( $\alpha$ ) and Sideslip Angle ( $\beta$ ) Profiles for Random Disturbances using Neuro-adaptive Generalized Dynamic Inversion

The angular angle and rate profiles are shown in Fig. 5.8 and Fig. 5.9 respectively. Minimal transients can be seen in all the plots because of Jacobian matrix learning. All the angular angle and rate profiles are converted into desired trajectories hence, the adaptive controller performance is maintained in presence of AHV model uncertainties. Therefore, the high fidelity model of AHV is not required. Finally, the adaptive control profiles are shown in Fig. 5.10, where all the trajectories are smooth and achievable.

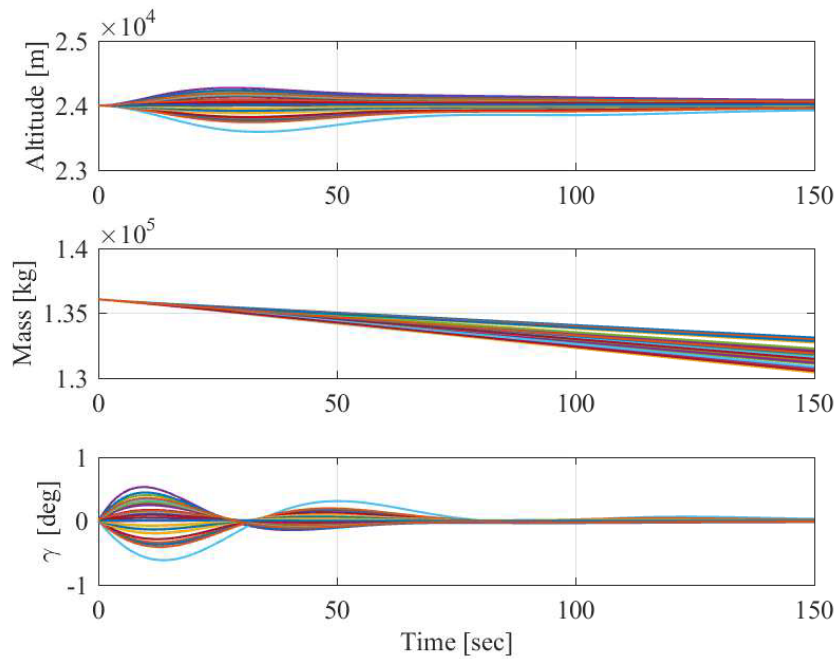


Figure 5.7 – Altitude ( $h$ ), Mass ( $M_v$ ) and Flight Path Angle ( $\gamma$ ) Profiles for Random Disturbances using Neuro-adaptive Generalized Dynamic Inversion

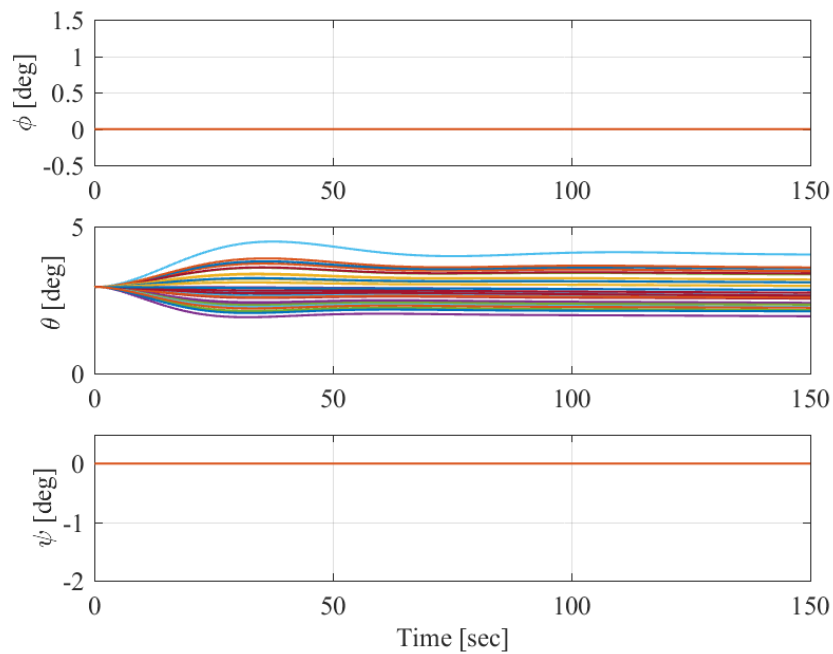


Figure 5.8 – Roll Angle ( $\phi$ ), Pitch Angle ( $\theta$ ), and Yaw Angle ( $\psi$ ) Profiles for Random Disturbances using Neuro-adaptive Generalized Dynamic Inversion

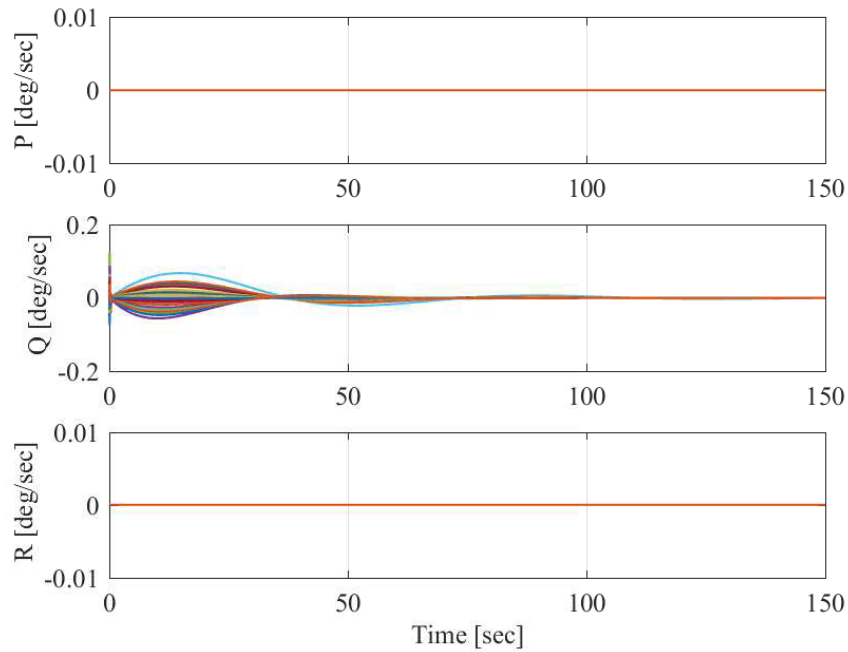


Figure 5.9 – Roll Rate ( $P$ ), Pitch Rate ( $Q$ ), and Yaw Rate ( $R$ ) Profiles for Random Disturbances using Neuro-adaptive Generalized Dynamic Inversion

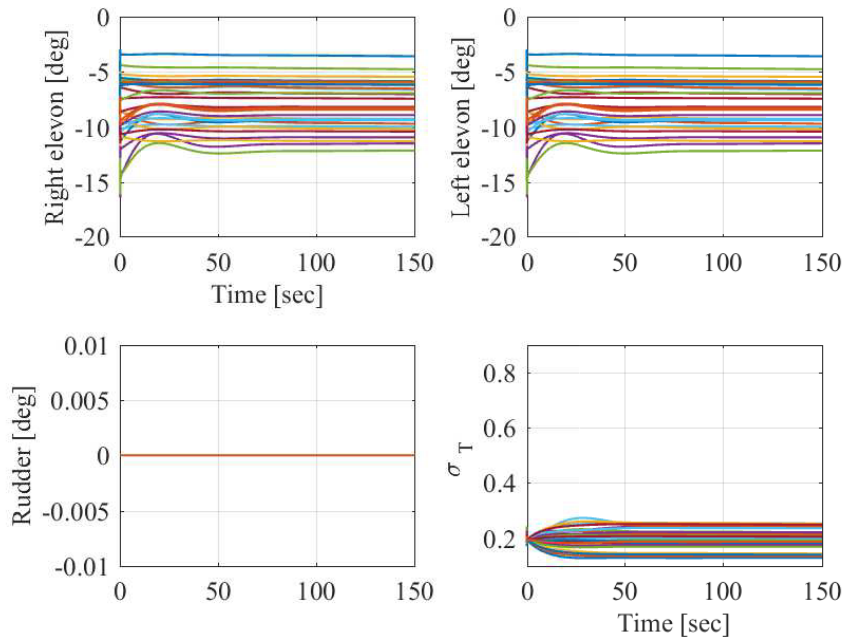


Figure 5.10 – Control Profiles obtained for Random Disturbances using Neuro-adaptive Generalized Dynamic Inversion

### 5.3 Quantitative Comparison Between Neuro-adaptive DI and GDI

In this section, the Monte-Carlo simulation results obtained from the application of neuro-adaptive DI and neuro-adaptive SC-GDI on the actual system is presented. To obtain the fair comparison, results are simulated for the same disturbances. The Monte-Carlo simulation results are shown in Table. 5.1, where, up to 30% disturbance, both control techniques works perfectly. However, as the disturbance increases, the SC-GDI proved slightly better than the DI because in SC-GDI technique the state constraint philosophy is used along with the constrained learning.

Table 5.1 – Quantitative Comparison Between Neuro-adaptive DI and GDI

<b>Model Un-certainties</b>	<b>Total Trials</b>	<b>SC-GDI: Successful Trials</b>	<b>Percentage of Success in SC-GDI</b>	<b>DI: Success-ful Trials</b>	<b>Percentage of Success in DI</b>
10 %	3697	3697	100 %	3697	100 %
20 %	3660	3660	100 %	3660	100 %
30 %	3602	3594	99.78 %	3580	99.39 %
40 %	3873	3455	89.2 %	3371	87.03 %

## 6 CONCLUSION

Two robust neuro-adaptive control design techniques are proposed in this report for the AHV in the cruise phase of flight. Further, an uncertain nonlinear winged-cone model is used to show the effectiveness of the derived controllers. First, DI controller is used to obtain the nominal control for the nominal system (no disturbance). The effectiveness of the nominal controller is shown by perturbed initial conditions.

Further, in presence of model uncertainties and disturbances, the robust neuro-adaptive DI controller is obtained by augmenting DI controller with proposed constraint disturbance learning algorithm. The applicability of the proposed control technique is shown by simulation results. Further, Monte-Carlo simulation results are also presented in the report.

A newly developed neuro-adaptive SC-GDI control technique is also proposed in this report for the robust control of uncertain AHV. BLF is used in the formulation of SC-GDI to obtain the state-constrained control. Further, SC-GDI control is augmented with the proposed constraint disturbance learning algorithm to formulate the neuro-adaptive SC-GDI control. Further, the effectiveness of the proposed neuro-adaptive SC-GDI control is validated by Monte-Carlo simulations.

Finally, It has been shown that both control techniques worked perfectly in presence of up to 30% model uncertainties and prevented inlet unstart along with the stabilization of the AHV. Hence, both neuro-adaptive DI and SC-GDI can be used to control the air-breathing hypersonic vehicle. Moreover, the high fidelity model of AHV is also not required.

# Bibliography

- Pradeep R Ambati and Radhakant Padhi. Robust auto-landing of fixed-wing uavs using neuro-adaptive design. *Control Engineering Practice*, 2016.
- Michael A Bolender and David B Doman. A non-linear model for the longitudinal dynamics of a hypersonic air-breathing vehicle. *AIAA paper*, 6255:2005, 2005.
- Michael A Bolender, Heidi Wilkin, Lance Jacobsen, Travis Drayna, and Andrew Dwenger. Flight dynamics of a hypersonic vehicle during inlet un-start. *AIAA Paper*, 7292:2009, 2009.
- Waseem Aslam Butt, Lin Yan, et al. Robust adaptive dynamic surface control of a hypersonic flight vehicle. In *49th IEEE Conference on Decision and Control (CDC)*, pages 3632–3637. IEEE, 2010.
- Gregory Errol Chamitoff. Robust intelligent flight control for hypersonic vehicles. ph. d. thesis-massachusetts inst. of technology. 1992.
- Andrew D Clark, Maj Dean Mirmirani, Chivey Wu, Sangburn Choi, and Matthew Kuipers. An aero-propulsion integrated elastic model of a generic airbreathing hypersonic vehicle. In *Proc. AIAA Guidance, Navigation, and Control Conf., AIAA Paper*, volume 6560, page 0, 2006.
- Colin C Coleman and Farhan A Faruqi. On stability and control of hypersonic vehicles. 2009.
- Richard Colgren, Shahriar Keshmiri, and Maj Mirmirani. Nonlinear ten-degree-of-freedom dynamics model of a generic hypersonic vehicle. *Journal of aircraft*, 46(3):800–813, 2009.
- HaiBin Duan and Pei Li. Progress in control approaches for hypersonic vehicle. *Science China Technological Sciences*, 55(10):2965–2970, 2012.



- Douglas Famularo, John Valasek, Jonathan A Muse, and Michael A Bolender. Enforcing state constraints on a model of a hypersonic vehicle. In *AIAA Guidance, Navigation, and Control Conference*, page 1865, 2016.
- Baris Fidan, Maj Mirmirani, and Petros A Ioannou. Flight dynamics and control of air-breathing hypersonic vehicles: review and new directions. *AIAA paper*, 7081(2003), 2003.
- Baris Fidan, Matthew Kuipers, Petros Ioannou, Maj Mirmirani, et al. Longitudinal motion control of air-breathing hypersonic vehicles based on time-varying models. In *14th AIAA International Space Planes and Hypersonic Systems and Technologies Conference, Canberra, AUS*, 2006.
- Travis E Gibson and Anuradha M Annaswamy. Adaptive control of hypersonic vehicles in the presence of thrust and actuator uncertainties. In *AIAA guidance, navigation and control conference and exhibit*, page 6961, 2008.
- LI Huifeng, LIN Ping, and XU Dajun. Control-oriented modeling for air-breathing hypersonic vehicle using parameterized configuration approach. *Chinese Journal of Aeronautics*, 24(1): 81–89, 2011.
- Alberto Isidori. *Nonlinear control systems*. Springer Science & Business Media, 2013.
- Shahriar Keshmiri, Maj D Mirmirani, and Richard Colgren. Six-dof modeling and simulation of a generic hypersonic vehicle for conceptual design studies. In *Proceedings of AIAA Modeling and Simulation Technologies Conference and Exhibit*, pages 2004–4805, 2004.
- Shahriar Keshmiri, Richard Colgren, and Maj Mirmirani. Development of an aerodynamic database for a generic hypersonic air vehicle. In *AIAA Guidance, Navigation, and Control Conference and Exhibit*, volume 6257. San Francisco, California, AIAA, 2005.
- Shahriar Keshmiri, Richard Colgren, and Maj Mirmirani. Six-dof modeling and simulation of a generic hypersonic vehicle for control and navigation purposes. In *AIAA guidance, navigation, and control conference and exhibit*, AIAA, 2006.
- Shahriar Keshmiri, Richard Colgren, and Maj Mirmirani. Six dof nonlinear equations of motion for a generic hypersonic vehicle. In *AIAA Atmospheric Flight Mechanics Conference and Exhibit*, pages 20–23, 2007.

- Matthew Kuipers, Petros Ioannou, Baris Fidan, and Maj Mirmirani. Robust adaptive multiple model controller design for an airbreathing hypersonic vehicle model. In *AIAA guidance, navigation and control conference and exhibit*, volume 7142, 2008.
- Christopher I Marrison and Robert F Stengel. Design of robust control systems for a hypersonic aircraft. *Journal of Guidance, Control, and Dynamics*, 21(1):58–63, 1998.
- Duane McRuer. Design and modeling issues for integrated airframe/propulsion control of hypersonic flight vehicles. In *American Control Conference, 1991*, pages 729–734. IEEE, 1991.
- Maj Mirmirani, Chivey Wu, Andrew Clark, Sangbum Choi, and Richard Colgren. Modeling for control of a generic airbreathing hypersonic vehicle. *AIAA paper*, 6256:2005, 2005a.
- Maj Mirmirani, Chivey Wu, Andrew Clark, Sangbum Choi, and Baris Fidan. Airbreathing hypersonic flight vehicle modeling and control, review, challenges, and a cfd-based example. In *Workshop on modeling and control of complex systems*, pages 1–15, 2005b.
- Radhakant Padhi, Nishant Unnikrishnan, and SN Balakrishnan. Model-following neuro-adaptive control design for non-square, non-affine nonlinear systems. *IET Control Theory & Applications*, 1(6):1650–1661, 2007.
- Wang Qian and Liu Jiaxue. A neural network adaptive inverse controller for hypersonic vehicle. In *2010 International Conference on Information, Networking and Automation (ICINA)*, volume 2, pages V2–240. IEEE, 2010.
- Elizabeth Rollins, John Valasek, Jonathan A Muse, and Michael A Bolender. Nonlinear adaptive dynamic inversion applied to a generic hypersonic vehicle. In *AIAA Guidance, Navigation, and Control (GNC) Conference*, page 5234, 2013.
- DK Schmidt. Integrated control of hypersonic vehicles. *AIAA paper*, pages 93–5091, 1993.
- Andrea Serrani, Alicia M Zinnecker, Lisa Fiorentini, Michael A Bolender, and David B Doman. Integrated adaptive guidance and control of constrained nonlinear air-breathing hypersonic vehicle models. In *2009 American Control Conference*, pages 3172–3177. IEEE, 2009.
- John D Shaughnessy, S Zane Pinckney, John D McMinn, Christopher I Cruz, and Marie-Louise Kelley. Hypersonic vehicle simulation model: winged-cone configuration. 1990.

- Jean-Jacques E Slotine, Weiping Li, et al. *Applied nonlinear control*, volume 199. prentice-Hall Englewood Cliffs, NJ, 1991.
- Keng Peng Tee and Shuzhi Sam Ge. Control of nonlinear systems with partial state constraints using a barrier lyapunov function. *International Journal of Control*, 84(12):2008–2023, 2011.
- Keng Peng Tee, Shuzhi Sam Ge, and Eng Hock Tay. Barrier lyapunov functions for the control of output-constrained nonlinear systems. *Automatica*, 45(4):918–927, 2009.
- Tyler J Vick. *Geometry Modeling and Adaptive Control of Air-Breathing Hypersonic Vehicles*. PhD thesis, University of Cincinnati, 2014.
- Qian Wang and Robert F Stengel. Robust nonlinear control of a hypersonic aircraft. *Journal of Guidance, Control, and Dynamics*, 23(4):577–585, 2000.
- Bin Xu and Yu Zhang. Neural discrete back-stepping control of hypersonic flight vehicle with equivalent prediction model. *Neurocomputing*, 154:337–346, 2015.
- Bin Xu, Danwei Wang, Fuchun Sun, and Zhongke Shi. Direct neural discrete control of hypersonic flight vehicle. *Nonlinear Dynamics*, 70(1):269–278, 2012.
- Zenghui Zhang, Lingyu Yang, Youwu Zhong, and Gongzhang Shen. Modeling and analysis for a generic hypersonic vehicle. In *Intelligent Control and Automation (WCICA), 2010 8th World Congress on*, pages 152–158. IEEE, 2010.